A trackable trinuclear platinum complex for breast cancer treatment

Nucleic Acids Research, 2025, **53**, gkaf628
https://doi.org/10.1093/nar/gkaf628
Chemical Biology and Nucleic Acid Chemistry

A trackable trinuclear platinum complex for breast cancer treatment

Sinéad O'Carroll[1,†], Creina Slator[1,†], Raphael E.F. de Paiva[1,†], Conor Newsome[1,†], Bethany Searle[1], Sriram KK[2], Sylvia Whittle[3], Thomas E. Catley[3], Stefano Scoditti[4,5,6], Katarzyna Mnich[7], Erica J. Peterson[8], Bin Hu[9], Jennifer E. Koblinski[9], Afshin Samali[7], Vickie McKee[1], Alice L.B. Pyne[3], Fredrik Westerlund[2], Nicholas P. Farrell[8,*], Andrew Kellett[1,*]

[1]School of Chemical Sciences, Dublin City University, Glasnevin, Dublin, D09 K20V, Ireland
[2]Department of Life Sciences, Chalmers University of Technology, Kemivägen 10, 412 96 Gothenburg, Sweden
[3]School of Chemical, Materials and Biological Engineering, University of Sheffield, Sheffield, S1 3JD, United Kingdom
[4]Department of Chemistry and Chemical Technologies, University of Calabria, Arcavacata di Rende (CS), 87036, Italy
[5]Donostia International Physics Center, Paseo Manuel de Lardizabal 4, Donostia 20018, Spain
[6]Polimero eta Material Aurreratuak: Fisika, Kimika eta Teknologia, Kimika Fakultatea, Euskal Herriko Unibertsitatea UPV/EHU, Paseo Manuel de Lardizabal 3, Donostia 20018, Spain
[7]Apoptosis Research Centre, University of Galway, Galway, H91 W2TY, Ireland Galway, Ireland
[8]Department of Chemistry, Virginia Commonwealth University, Richmond, VA 23284-2006, United States
[9]The Massey Cancer Center, Virginia Commonwealth University, Richmond, VA 23298-0037, United States

[*]To whom correspondence should be addressed. Email: andrew.kellett@dcu.ie
Correspondence may also be addressed to Nicholas P. Farrell. Email: npfarrell@vcu.edu
[†]The first four authors should be regarded as Joint First Authors.

Abstract

Cancer remains a leading cause of death, with triple-negative breast cancer (TNBC) being particularly significant due to limited treatment options. As such, there is interest in anticancer polynuclear platinum(II) complexes, attributed to their unique DNA-binding modes and potential against therapy-resistant cancer phenotypes. However, a persistent challenge with polynuclear compounds is their lack of cellular trackability, hindering their effectiveness and monitoring in clinical settings. Here, we report the preparation of a new azide-appended trinuclear platinum complex, N_3-TriplatinNC, and characterize its DNA-targeting, cytotoxicity, and topoisomerase relaxation properties from the nanoscale to the macroscale. Using single-molecule biophysics and in-liquid atomic force microscopy, N_3-TriplatinNC was identified as a powerful DNA recognition agent with remarkable potential towards the TNBC cell line, MDA-MB-231. Installation of the azide handle on the polynuclear complex was achieved using a first-in-class approach to produce a complex that retained analogous biological activity to the parent TriplatinNC. Importantly, the azide handle facilitates *in situ* click chemistry for tracking cellular localization, with subsequent xenograft studies demonstrating *in vivo* antitumoural potential.

Graphical abstract

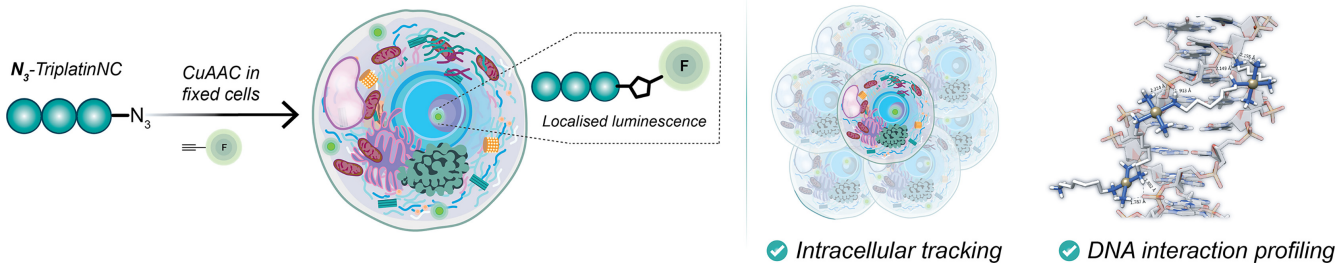

Introduction

Mononuclear *cis*-chemotype platinum(II)-based drugs have held an essential role in chemotherapy since the discovery [1] and subsequent FDA approval of cisplatin in 1978. Platinum-based chemotherapies remain a critical component in the treatment of many solid epithelial human cancers and constitute one of the most important and widely applied drug classes in clinical use [2]. While the use of cisplatin (Fig. 1A)

Received: October 15, 2024. **Revised:** June 11, 2025. **Editorial Decision:** June 11, 2025. **Accepted:** June 23, 2025

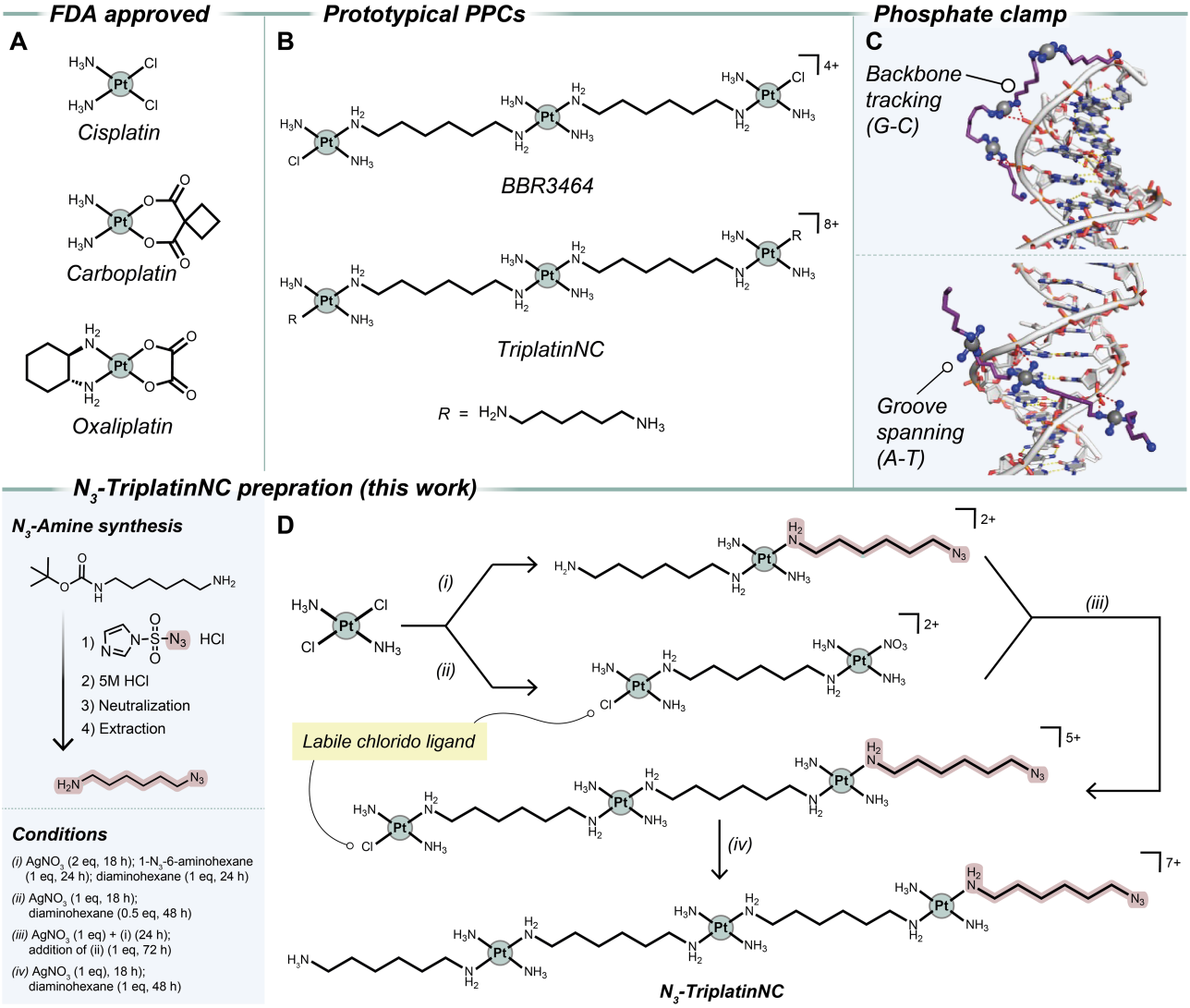

Figure 1. (**A**) Worldwide FDA clinically approved platinum(II) drugs cisplatin, carboplatin, and oxaliplatin along with (**B**) prototypical polynuclear platinum(II) compounds (PPCs) BBR3464 and TriplatinNC. (**C**) X-ray structures showing the noncovalent DNA-binding modes of TriplatinNC: groove spanning and backbone tracking (PDB: 2DYW). (**D**) Synthetic route for N_3-TriplatinNC: in route (i) the preparation of N_3-MonoplatinNC is shown while in route (ii) the isolation of the mono-activated di-nuclear platinum(II) 1,1/t,t, complex was achieved. Combining both precursors in step (iii) generates the mono-activated triplatinum(II) precursor to the target N_3-TriplatinNC formed in step (iv). Synthetic route for the preparation of the 1-azido-6-amino hexane linker is shown (inset).

has dramatically improved mortality rates and revolutionized cancer treatment, the drug does not come without limitations such as systemic toxicity and inherent resistance [3]. Recent work has therefore focused on the development of new platinum(II) chemotherapeutics with alternative mechanisms of action [4] and targeted DNA-binding modes [5] with the hope of overcoming traditional platinum(II) resistance. To this end, there has been a major drive toward the discovery and therapeutic application of the polynuclear platinum(II) compounds (PPCs). The PPCs, exemplified by trinuclear agents BBR3464 [6] and TriplatinNC [7] (Fig. 1B), demonstrate an ability to overcome cisplatin-resistance *in vitro* and *in vivo* due to each of their unique DNA binding motifs [8, 9]. BBR3464 was the first, and remains the only platinum(II) agent to enter clinical trials not based on the conventional mononuclear *cis*-chemotype and was designed to afford long range DNA crosslinking that circumvents the upregulated damage/repair mechanisms associated with 1,2-intrastrand crosslinking [10]. Despite its substantial toxicity to tumour cells, the compound did not progress beyond phase II clinical trials, partially due to its decomposition in human serum into inactive mononuclear platinum units [11].

TriplatinNC, in principle a substitution-inert trinuclear PPC, was discovered to have a discrete DNA-binding mode now known as the phosphate clamp [7]. The phosphate clamp shows selective hydrogen-bonding involving am(m)ines surrounding each platinum(II) centre and phosphate oxygens of the anionic DNA backbone. Recent work by Farrell, Kellett, and co-workers identified two sequence-dependent binding motifs of the phosphate clamp: backbone tracking observed on GC-rich DNA, and groove-spanning across the minor groove of AT-rich DNA (Fig. 1C) [12, 13]. Previously, TriplatinNC's cellular internalization and resulting cell cycle arrest has been studied using nanoscale secondary ion mass spectroscopy (NanoSIMS) in human breast adenocarcinoma (MCF-7) using ^{195}Pt and ^{15}N as target markers [14,

15]. Fluorescent tagging using a 7-nitro-2,1,3-benzoxadiazole appended derivative of TriplatinNC later revealed nucleolar localization in A2780 cells [16]. However, it is axiomatic that tethering a bulky fluorophore to a platinum(II) drug prior to cell exposure may influence localization and targeting properties. An elegant strategy by DeRose and coworkers for studying mononuclear platinum(II) drugs *in vitro* and *in cellulo* involves the installation of bioorthogonal handles—either azides or alkynes—onto the platinum scaffold, enabling post-treatment conjugation with complementary fluorogenic probes via click chemistry [17–19]. This 'post-labelling' strategy was enabled by click chemistry due to its bio-orthogonality, broad scope, high selectivity, and efficiency. As yet, no methodology has been established to achieve the intracellular tracking of polynuclear platinum compounds and how this might differ from the neutral cisplatin chemotype.

Here, we present the synthesis, characterization, DNA interaction, *in vitro* and *in vivo* cytotoxic response, broad spectrum anticancer activity within the National Cancer Institute 60 human tumour cell line screen (NCI-60), and cellular localization studies of an entirely new azide-appended TriplatinNC (N_3-TriplatinNC). The azide handle facilitates *in situ* click conjugation to an alkyne-modified fluorophore for applications in visualizing the native intracellular localization properties of PPCs by confocal microscopy. To determine whether the terminal azide group on N_3-TriplatinNC preserves the DNA recognition and downstream biological activity of its parent compound, TriplatinNC, we conducted a comprehensive series of nucleic acid binding experiments spanning across nano- to macroscale dimensions. Overall, the remarkable results obtained within the DNA recognition and cytotoxic analyses identified this trackable polynuclear platinum compound as a promising nucleolar-targeting chemotherapeutic for treating triple-negative breast cancer (TNBC).

Materials and methods

For the full synthetic procedures and characterization data of all compounds developed in this study, see the Supplementary Information. All materials generated were synthesized using reagents purchased from Sigma–Aldrich (Ireland) or Tokyo Chemical Industries (TCI, UK Ltd) and used for the synthesis and preparation of organic ligands and metal complexes without purification. All platinum(II) complexes were synthesized as nitrate salts.

NMR

Nuclear magnetic resonance (NMR) experiments were conducted at room temperature using either using D_2O obtained from Deutero GmbH or $CDCl_3$ obtained from Merck KGaA. Solvents were used without further purification. All NMR data were obtained on a Bruker Avance Ultrashield 600 MHz instrument. Intermediates were analysed by ^{1}H NMR and all final products by ^{1}H NMR, ^{13}C NMR, DEPT, and ^{195}Pt NMR. All spectra are contained in supplementary information (Supplementary Section S1.4, Supplementary Figs S3–S6). Data were processed and analysed using Mnova software.

Infrared

All infrared (IR) data were collected at room temperature using a Perkin Elmer Spectrum Two FT-IR (Fourier Transform-Infrared) Spectrometer (Supplemental Section S1.5, Supplementary Fig. S7). Data were processed and analysed using GraphPad Prism (V10.1.1).

High performance liquid chromatography

Analyses were carried out on a Shimadzu Prominence system with Nexera X2 photo-diode array detector module. A Bio-Rad Bio-Sil Sec 400–5, 300 mm × 7.8 mm was used with a gradient elution method solvent A: H_2O/ACN 60/40; solvent B: 95/5. Samples were prepared as 1 mg/ml solutions in high performance liquid chromatography (HPLC) grade H_2O. The injection volume was 50 µl and flow rate was kept constant at 1.5 ml/min for 60 min. (Supplemental Section S1.6, Supplementary Fig. S8)

Mass spectrometry

Mass spectra were recorded using electrospray ionization on a Bruker microTOF-Q II spectrometer (nanospray, capillary temperature = 180°C, spray voltage = 3.7 kV) and were dissolved in water and diluted in acetonitrile. Due to the high charge and long chain ligands, ligand displacement, and the resulting charge difference is observed providing a larger number of possible fragmentation patterns. Three major fragments were identified: (i) a triplatinum species containing the dangling azide; (ii) a monoplatinum species containing the dangling amine present; (iii) a similar monoplatinum species containing the dangling amine with different degrees of amine displacement due to presence of solvent and different ionic species. (Supplemental Section S1.7, Supplementary Fig. S9-S10)

Elemental analysis

Samples were analysed using a Flash EA Elemental Analyser and Eager 300 software. A total of 2–4 mg of sample was placed in a tin capsule and pyrolyzed at a temperature >1000°C with a portion of O_2 gas. The resultant gases were passed through a quartz reactor tube containing copper/chromium oxide and silvered cobaltous oxide where they are purified and reduced. The emerging gases were separated on a PTFE Multiseparation Column and detected using a thermal conductivity detector. The percentage of carbon, nitrogen and hydrogen was determined from the resulting chromatographic peaks. The carrier gas used was helium at a rate of 130 ml/min and a run time of 530 s. The instrument was calibrated before use against a certified nicotinamide standard. Note: the discrepancy between the calculated and experimentally determined nitrogen content in azide–platinum(II) complexes was attributed to the thermal instability of the azide moiety under the combustion conditions employed during elemental analysis.

Chemical synthesis

Synthesis of N_3-MonoplatinNC

Transplatin (0.210 g, 0.70 mmol) was dissolved in anhydrous DMF (dimethylformamide; 10 ml), treated with silver nitrate (0.239 g, 1.40 mmol) and stirred for 18 h, at room temperature, shielded from light. The precipitated silver chloride was filtered off and filtrate cooled to −30°C. A solution of 1-amino-6-azido hexane (0.100 g, 0.70 mmol, see Supplemental Section S1) in DMF (15 ml) was added dropwise to the cooled filtrate over 1 h and allowed stir for 48 h, at

room temperature, shielded from light. The reaction mixture was cooled to −30°C and added with a solution of 1,6-hexane diamine (0.082 g, 0.70 mmol) in DMF (15 ml) over 2 h and allowed stir for 24 h shielded from light. Volume of solvent was reduced to ∼5 ml, diluted with Et_2O (500 ml) and allowed stir for 30 min on ice before filtering. The filter cake was washed with ice-cold Et_2O. Yield 0.272 g (68%). ^{1}H NMR (600 MHz, D_2O): δ = 3.28 ppm (t, 2H), 2.94 ppm (m, 2H), 2.62 ppm (m, 4H), 1.62 ppm (m, 8H), 1.35 ppm (m, 8H). ^{195}Pt NMR (600 MHz, D_2O): δ = −2664 ppm. Elemental analysis calculated (%) for $C_{12}H_{36}N_{10}O_6Pt$: C 23.57, H 5.93, N 22.90; found: C 22.48, H 5.23, N 18.75. IR (ATR cm^{-1}): 3220, 3140, 2931, 2860, 2097, 1606, 1307, 1041, 825.

Synthesis of N_3-TriplatinNC

Intermediate 1,1/t,t (0.080 g, 0.11 mmol, see Supplementary information) was dissolved in anhydrous DMF (15 ml), treated with silver nitrate (0.018 g, 0.10 mmol), and stirred at room temperature overnight shielded from light. The precipitated silver chloride was filtered off and the filtrate cooled to −30°C. A solution of N_3-monoplatinNC (0.064 g, 0.11 mmol) in DMF (15 ml) was added dropwise to the filtrate over 2 h and stirred for 72 h at room temperature. The solution was filtered to remove any traces of reduced platinum. The filtrate was treated with silver nitrate (0.018 g, 0.10 mmol) and stirred over night at room temperature, shielded from light. The precipitated silver chloride was filtered off and the filtrate cooled to −30°C. A solution of hexamethylene diamine (0.012 g, 0.11 mmol) in DMF (5 ml) was added dropwise to the filtrate over 1 h and subsequently stirred for 2 days at room temp. The product was precipitated out of solution using Et_2O (400 ml), filtered and the filter cake washed with ice-cold Et_2O. Yield: 0.104 g (63%). ^{1}H NMR (600 MHz, D_2O) δ 3.35–3.23 (m, 2H), δ 2.80–2.73 (m, 6H), 2.67–2.65 (m, 8H), 1.69–1.61 (m, 10H), 1.56–1.54 (m, 6H), 1.40–1.34 (m, 16H). ^{195}Pt NMR (600 MHz, D_2O): δ = −2671 ppm. Elemental analysis calculated (%) for $C_{24}H_{80}N_{22}O_{18}Pt_3$: C 18.59, H 5.20, N 19.88; found: C 19.14, H 5.13, N 16.21. IR (ATR cm^{-1}): 3213, 3153, 2933, 2863, 2099, 1655, 1603, 1307, 1038, 826 (see Supplementary Section 1.5. for mass analysis).

Single molecule nanofluidics

Sample preparation

TriplatinNC and N_3-TriplatinNC were dissolved in water to 500 μM stock concentration. The stocks were further diluted to 10 μM and used in preparing DNA–drug complexes for the single-molecule experiments. Reaction mixtures containing 4.8 μM (base-pairs) bacteriophage λ-DNA [48 502 base pairs, New England Biolabs (NEB), USA] and varying concentrations of TriplatinNC or N_3-TriplatinNC were prepared and incubated at room temperature for 15 min. After incubation, 0.5 μl of 10 μM YOYO-1, a nonspecific bis-intercalating fluorescent dye (1:10 dye:bp ratio, Invitrogen, USA), and 0.5× Tris-borate-ethylenediaminetetraacetic acid buffer (TBE; Sigma–Aldrich, USA) were added to the DNA–drug mixture to obtain a final volume of 10 μl. This mixture was incubated again at room temperature for 15 min to enable fluorescence staining of the DNA molecules by YOYO-1. This mixture was then diluted with 39 μl of Milli-Q water (18.2 MΩ ionic purity, Millipore, USA) and 1 μl of β-mercaptoethanol (BME; Sigma–Aldrich, USA) to yield a 50 μl loading solution.

For the intensity profile comparison of λ-DNA molecules treated with TriplatinNC and N_3-TriplatinNC and labelled with YOYO-1 dye, a reference profile using YOYO-Netropsin one-step competitive binding was used. Netropsin is known to bind to AT-rich regions of DNA, thus leaving only the GC regions for the YOYO-1 dye to bind, creating an intensity profile with bright YOYO-1 bound regions and dark netropsin bound regions along the nanochannel-stretched DNA [20–22]. For this, λ-DNA (4.8 μM base-pairs) was incubated with YOYO-1 (10 μM) and netropsin (100 μM, Sigma–Aldrich) and 0.5× TBE buffer was added to a final volume of 10 μl. This mixture was incubated at 50°C for 30 min, to achieve homogeneous staining of all DNA molecules. Before fluorescence imaging, this solution was diluted ten times with Milli-Q water containing 3% (*v*/*v*) of BME to a total volume of 100 μl.

Nanofluidic device

For single molecule experiments using nanofluidics, a device that consists of two microfluidic channels, each connecting two loading reservoirs was used. Spanning across the microfluidic channels are 200 nanofluidic channels. Each nanochannel is 150 nm in width, 100 nm in depth, and 500 μm in length, and the spacing between two consecutive nanofluidic channels is 800 nm. All devices were made in silicon wafers (Si-Mat, Germany) with a 2 μm thick thermal oxide, using traditional semiconductor fabrication processes in a cleanroom facility. Microchannels were fabricated using photolithography (S1813; Shipley Inc., USA) and reactive ion etching (RIE, Oxford Instruments, UK), whereas the nanofluidic channels were formed using electron beam lithography (JEOL JBX-9300FS, Japan) and RIE. Loading reservoirs were etched using deep RIE (STS-ICP) and finally the microfluidic and nanofluidic confinements were obtained by high temperature bonding of borosilicate glass (170 μm thick, double side polished, Si-Mat, Germany) to the silicon wafer. Detailed description of the fabrication steps involved can be found in earlier studies by Westerlund and co-workers [23, 24].

Each nanofluidic chip was mounted on a plastic frame, which was then mounted on a custom-built chuck to enable pressure-driven flow and mounted on an epi-fluorescence microscope. Fifteen microlitres of the loading solution was pipetted to one of the four loading reservoirs, while the remaining three reservoirs were filled with 0.05× TBE buffer with 2% (*v*/*v*) BME. First, an N_2-pressure was applied to drive the DNA molecules from the reservoir it was loaded in to the connected microchannel. Once the microchannel was filled with DNA molecules (∼30 s), an N_2-pressure was applied across the nanochannels, to push the DNA molecules into the nanochannels. Once the DNA molecules were in the nanochannels, pressure was turned off to keep the DNA molecules within the nanochannels for imaging.

Imaging and analysis

Images were collected using an inverted fluorescence microscope (Axio Observer Z1, Carl Zeiss AG, Germany) illuminated with a Colibri 7 LED light source (Carl Zeiss AG, Germany) with a 512 × 512 pixels, 16 μm^2 EMCCD camera (Photometrics evolve, Teledyne Photometrics, USA). A total of 20 frames (100 ms each) were collected for each image stack. A FITC (fluorescein isothiocyanate) filter (470/20 nm excitation and 530/50 emission) was used. The .czi files were

converted into .tiff files using a macro in ImageJ. Custom-made Matlab codes were used for further image processing and analysis [20,25]. Briefly, kymographs were generated from single DNA molecules stretched in the nanochannels and these kymographs were used for measuring the end-to-end extension of the DNA molecules and also to obtain the DNA intensity profiles from TriplatinNC/N_3-TriplatinNC and YOYO-1 binding. Concentric plots showing the DNA barcode of tens of λ-DNA molecules was obtained to visualize if the intensity patterns formed by TriplatinNC or N_3-TriplatinNC and YOYO-1 were consistent across many DNA molecules or of random nature.

Topoisomerase I (Topo IA) relaxation assay

The interaction between N_3-TriplatinNC bound to duplex DNA and Topoisomerase IA was assayed using agarose gel electrophoresis, following the most recent NEB protocol and recommendations (https://www.neb.com/en-gb/protocols/2018/08/30/protocol-for-topoisomerase-i-ecoli-m0301). Briefly, 20 μl samples containing 400 ng of pUC19 plasmid DNA and increasing concentrations of either N_3-TriplatinNC or TriplatinNC (ranging from 0.1 to 30 μM) in media containing 1× rCutSmart and 80 mM HEPES (4-(2-hydroxyethyl)piperazine-1-ethanesulfonic acid) buffer pH 7.2 were incubated at 37°C for 30 min. Subsequently, Topo IA (1 U) was added and samples were incubated at 37°C for 15 min. The enzyme was heat inactivated by incubation at 65°C for 30 min. DNA loading buffer was added to each sample to 1× dilution (4 μl from a 6× stock), and samples were loaded onto a 1.2% agarose gel cast for 20 samples. A negative control (DI water instead of Topo IA) and a positive, untreated control (pUC19 exposed to Topo IA in the absence of platinum drugs) were also run along with treated samples. Electrophoretic separation of the topoisomers was achieved in 1× TBE buffer by running at 40 V for 3 h followed by 50 V for 3 h. The gel was stained post-separation by soaking in 1× SYBR Safe (diluted from a 10 000× stock in dimethyl sulfoxide (DMSO)) in 1× TBE overnight. Images were acquired in G:BOX Mini 9 Multi-Application Gel Imaging System.

Microscale thermophoresis

A 10 μl working solution of 0.2 μM hairpin DNA, G-C rich sequence F-TP, and A-T rich sequence F-D6aH tagged with a 5′-Cy5 fluorophore, was prepared in 200 mM HEPES, 25 mM NaCl. N_3-TriplatinNC was dissolved in H_2O with 10% DMSO and further diluted to 13.3 μM using the HEPES buffer to form a stock solution. A total of 17 samples were prepared with 10 μl of the HEPES buffer and a serial dilution of N_3-TriplatinNC was then performed in a 3:1 [drug]/[buffer] ratio, providing a working concentration range of 10 μM to 75 nM. DNA (F-TP/F-d6AH, 10 μl) was then added to each sample providing a final concentration range of 5 μM to 37.5 nM of drug. These samples were then incubated at 37°C for 1 h. NanoTemper premium capillaries were placed into each sample and left until liquid had filled the capillary, care was taken to avoid touching the centre of the capillaries. The capillaries were then placed into the 'NanoTemper Technologies (GmbH, MO-K022) Monolith' MST instrument and scanned using high power and auto-excitation in the red channel. The above method was repeated for F-D6aH to afford a final concentration range of 10 μM–75 nM of drug. The data were then opened on The MO.Affinity Analysis software (NanoTemper Technologies GmbH) before being exported to Graphpad Prism for analysis.

High-resolution in-liquid Atomic Force Microscopy (AFM)

Sample preparation for AFM

Selected samples, prepared in the same way as described in the Topoisomerase IA relaxation assay, were imaged using high resolution in-Liquid AFM. Namely, the selected samples were those containing 0.75, 1.0, 2.5, and 5.0 μM N_3-TriplatinNC; and 1.0, 2.5, 5.0, and 7.5 μM TriplatinNC. The incubated samples (20 ng/μl) were prediluted to 4 ng/μl (20 μl) and immobilization on freshly cleaved mica following a published protocol [26]. A total of 20 μl of immobilization buffer (25 mM $MgCl_2$ in 10 mM tris pH 7.4) was applied to mica, followed by pipetting of 10 μl of the prediluted sample and gentle homogenization of the droplet by pipetting. The sample was left undisturbed for 5 min at room temperature, followed by 3× washing of the surface with 20 μl imaging buffer (3 mM $NiCl_2$ in 20 mM HEPES pH 7.4). Samples were left undisturbed for 20 min at room temperature before imaging. A sample containing 5 μM TriplatinNC and 400 ng pUC19, without exposure to Topo IA was also prepared in an analogous way. This sample was subjected to consecutive imaging rounds and provided dynamic information about the intramolecular condensation of plasmid DNA induced by PPCs.

AFM imaging

All AFM measurements were performed in liquid following a published protocol [26]. Imaging was carried out in PeakForce Tapping mode on a FastScanBio AFM, using FastScanD probes (Bruker). The PeakForce Tapping amplitude was set to 10 nm, the PeakForce Tapping frequency to 8 Khz and the PeakForce setpoints in the range: 7–15 mV, corresponding to peak forces of <70 pN. Images were recorded at 512 × 512 pixels at line rates of ∼3 Hz.

AFM image processing

All AFM images were processed and analysed using TopoStats [27], a Python pipeline for the automated processing and analysis of AFM data (https://github.com/AFM-SPM/TopoStats). TopoStats can be configured using a configuration file. In this instance, the default settings were used with three changes. First, the upper threshold for the filtering and grain detection stages was changed depending on the sample type in order to obtain the highest quality flattening, and secondly the height range for the images was set to [−3, 4] in order to produce images where height differences were more easily visible. The absolute area thresholds were also adjusted in order to ignore noise and anomalies of varied size in the data. The configuration file can be found with the dataset. Processing was carried out using the following steps: an initial flatten was conducted to remove image tilt by subtracting a plane, and to remove line-to-line variation from the raster scan process by subtracting the median of each row, and to remove bowing effects by subtracting a horizontal quadratic polynomial. Scar removal was then run on the flattened image, detecting and linearly interpolating any significantly high or low one-to-four-pixel wide horizontal streaks in the image.

Masking was then performed to select the molecules within the image by calculating a height threshold to separate the background from the data in the image. The threshold was

calculated from the standard deviation of the image, multiplied by a scaling factor. Regions of the image that lay above the threshold were considered to be molecules, referred to as grains, and isolated as a binary mask. The original image was then flattened again, excluding the grains from the calculation of the median for each row, plane fit and quadratic fit. This improved the flattening of the image, ensuring the background was as flat as possible. The height distribution of the flattened image was then shifted vertically to set the background, i.e. mica height, to zero by calculating the mean of the nongrain containing data and subtracting that value from the image. Finally, a gaussian blur of sigma = 0.5 pixels was applied to reduce high frequency noise in the image. To analyse individual molecules, connected-component labelling was applied to the binary mask to label unique grains, which were then filtered by size to remove noise or small contaminants that were erroneously detected as grains. Grains that intersected with the border of the image were also removed due to the impossibility of accurately calculating statistics for them. This resulted in a labelled binary mask that used for statistical analysis. A set of statistics was calculated for each grain, including but not limited to aspect ratio, area, volume, minimum and maximum feret diameters, and average height. The minimum and maximum feret diameters and minimum bounding area are plotted in Fig. 4.

Biological assays

DNA binding data

For the full materials, methods, instrumentation and analysis of all compounds developed in this study, see the Supplementary Information.

Cell culture and treatments

MCF-7, MDA-MB-231, and MDA-MB-468 cells were maintained in high glucose Dulbecco's modified Eagle's medium (DMEM) and T47D were maintained in RPMI-1640. All media were supplemented with 10% FBS (fetal bovine serum), 1% L-glutamine, and 50 units/ml penicillin and 50 mg/ml streptomycin. MCF-10a were cultured in DMEM/F-12 supplemented with 5% horse serum, 20 ng/ml epidermal growth factor, 100 ng/ml cholera toxin, 0.01 mg/ml insulin, and 500 ng/ml hydrocortisone. Cells were maintained at 37°C and 5% CO_2 in a humidified atmosphere. Complex stock solutions were prepared in 0.9% saline (*w*/*v*). Cisplatin was stored at 4°C for up to 1 week while all other stocks were kept as frozen aliquots. Further dilutions were prepared in culture media daily.

Cell viability assay

Seeding densities and resazurin (alamar blue) incubation times were predetermined based on Z-score analysis (>0.6). MCF-7, MDA-MB-231, MDA-MB-468, and MCF-10a cells were seeded at 5000 cells per well in a 96-well plate, while T47D cells were seeded at 7500 cells per well for 18 h prior to drug treatment. Cells were exposed to platinum complexes at 1–100 μM using an automated liquid handling system (JANUS Automated Workstation) and incubated for 24 or 48 h. A 1:10 dilution of resazurin reagent (stock concentration of 5.6 mM, Sigma R7017) was added and incubated for a further 4 h (MCF-7) or 6 h (MDA-MB-231, MDA-MB-468, T47D, and MCF-10a). Fluorescence was measured on an integrated Victor ×5 Multilabel Reader (ex: 530 nm, em: 620 nM). Cell viability was expressed as normalized percent of viable cells relative to nontreated control and IC_{50} values were calculated in GraphPad Prism (Supplementary Table S4).

Confocal analysis for N_3-TriplatinNC localization

MDA-MB-231 cells were treated with 5–10 μM N_3-TriplatinNC for 24 or 48 h then stained with 150 nM MitoTracker Deep Red for 20 min at 37°C. Cells were fixed in 4% paraformaldehyde (30 min, RT) and permeabilized with 0.25% Triton X-100. Samples were then blocked with 2% bovine serum albumin for 30 min at RT and clicked with 1:1 equivalent of Fluor 488-alkyne in the presence of $CuSO_4$ (10 mM) and ascorbate (20 mM) for 30 min at RT (room temperature) and then counter-stained with NucBlue Fixed. Specific localization protein, nucleophosmin (NPM), was stained to investigate nucleolar localization. The primary antibody (anti-B23 antibody, mouse monoclonal antibody, B0556-25UL, Merck) was incubated at 1:500 dilution, RT for 2 h followed by secondary antibody (Alexa Flour 594 goat antimouse IgG F(ab)2 fragment, A11020; Thermo Fisher Scientific) at 1:1000 dilution, RT for 1 h. Cells were washed twice with phosphate-buffered saline (PBS) in between each step. Samples were finally mounted in ProlongGold and allowed to cure. Confocal samples were imaged on a STED-Leica DMi8 super resolution confocal microscope equipped with a CCD (charge-coupled device) camera. NucBlue Fixed was excited with a 405 nm picoquant laser unit and emission captured between 450 and 550 nm. Fluor 488-alkyne (≡−488) was excited at 488 nm (laser power 1) with emission captured between 580 and 625 nm, and MitoTracker Deep Red was excited at 637 nm (laser power 3) with emission was captured at 650–700 nm. Alexa Flour 594 conjugated secondary antibody was excited at 594 nm (laser power 5) with emission was captured at 640–680 nm. Images were acquired whereby combinations of excitation and emission wavelengths for specific dyes were applied sequentially to avoid overlap between photophysical profiles.

National Cancer Institute 60 cell line screening

N_3-TriplatinNC (NSC: 843 992) was submitted to the US National Cancer Institute's (NCI) Developmental Therapeutics Program (DTP) 60 human cancer cell line screening. The cytotoxic or lethal effects (50% lethal dose, LC_{50}) growth inhibition (GI_{50}) and total growth inhibition (TGI) were identified using a five-dose exposure level and are shown in the raw result data (Supplementary Table S5). These results are categorized by cancer type and then visualized in a heat map as shown in Supplementary Fig. S30, with the lowest concentration of 0.5 μM, and the highest 85 μM. The panel consists of 60 human cancer cell lines from including breast, colon, central nervous system, leukaemia, nonsmall cell lung, melanoma, ovarian, prostate, and renal cancers. COMPARE algorithm analysis is detailed in the Supplementary Section 3.2.

Maximum tolerated dose

Animal work carried out in Virginia Commonwealth University (VCU), USA. Both toxicity and xenograft studies were approved by VCU Institutional Animal Care and Use Committee (IACUC/ Animal Welfare License AD10000943). All research involving animals were conducted in strict accordance of the Animal Welfare Act and regulations as amended (Public Law 99–198: The Improved Standard for Laboratory Animals Act, and Public Law 103–43: Plan for Use of Animals in Research).

Female NCG mice (NOD CRISPR Prkdc Il2r gamma) of 6–8 weeks old and weighing ∼20 g were purchased from Charles Rivers Laboratories. NCGs are coisogenic immunodeficient models achieved through CRISPR knockout which can host xenograft cells as they lack proper T-cell and B-cell formation and NK (natural killer) cells. Acute toxicity analysis was used to determine the maximum tolerated dose of the drug, which was administrated *via* intraperitoneal injection at 1, 5, and 10 mg/kg in 100 µl saline in three animals per group previously randomized based on body weight on days 1, 5, and 9. Tolerance of dose and the health of the animals were continuously monitored for a further 15 days and represented as relative body weight. No decrease in body weight was observed for all animals administered with the compound and a dose of 5 mg/kg was selected for further analysis.

Xenograft studies

MDA-MB-231-*luc* cells were cultured in DMEM media supplemented with 10% FBS, 1% L-glutamine, and 1% penicillin/streptomycin. Cells already provided in VCU were generated by infection with lentiviruses containing the pFULT vector expressing fire-fly luciferase. MDA-MB-231-*luc* cells (2×10^4) in a PBS:matrigel mixture were injected into the forth right lactiferous duct of 6–8 weeks old female mice. Animals were monitored for 1 week after which tumour growth was visualized *via* IVIS (*in vivo* imaging system) imaging by injecting 100 µl of luciferin subcutaneously, waiting 10 min and using inhalant isoflurane to anaesthetize the animals. Mice were randomized to five animals per group when tumour volumes reached 50 mm^3 on day 10. Animals per group were randomized on the basis of tumour volume (obtained using a digital calliper and IVIS imaging) and body weight through randomization Multi-Task program as described by Hampton *et al*. [28]. MDA-MB-231 *luc* cells (2×10^4) were implanted through intraductal injection into the mammary glands of NCG mice. Tumours started to develop and were allowed to grow to a minimum volume of 50 mm^3. Tumour size was manually measured as volume and quantified using luciferin bioluminescence where MDA-MB-231 cells were transfected with a recombinant vector resulting in luciferase expression. Cells were then injected with D-luciferin which reacted with luciferase to generate a chemiluminescent reaction. The luminescent flux of photons generated in the tumour was detected through next-generation bioluminescence optical *in vivo* imaging known as IVIS. Mice were then randomized to groups of five and treated with saline vehicle in the negative control cohort, 5 mg/kg of N_3-TriplatinNC or 40 mg/kg of positive control carboplatin as an established clinical agent, and then monitored for a further 20 days. Mice were euthanized when tumour size impeded the welfare of the animals (including drug treated mice).

Ethics statement

The animal study was carried on VCU IACUC approved protocol #AD10000943. VCU Cancer Mouse Models Core (CMMC) uses 2.5% vaporized isoflurane gas mixed with oxygen at 2 LPM flow rate to anaesthesia during the procedures. CO_2 Asphyxiation plus Cervical Dislocation is used for animal euthanasia at VCU CMMC. Mice were monitored for clinical signs secondary to tumour burden, including laboured breathing or increased respiration, weight loss >20% or tumour burden >2000 cubic millimeter (weigh at least once a week), body condition score of <2, scruffy hair coat, hunched posture, 3+ (slow to move when prodded) out of 5 on an activity scale, and interference with normal body functions such as eating, drinking, defecation, or urination. If any of these signs occur, the animals are euthanized. We employed IVIS imaging to assess objective tumour burden when the tumours express luciferase, otherwise, we use only caliper measurement; however, the animals' overall well-being takes priority over precise tumour measurements when considering euthanasia or other interventions.

Results and discussion

Synthesis of azido-TriplatinNC (N_3-TriplatinNC)

The synthesis of any platinum(II) molecule is directed by the *trans* effect, which is defined as the ability of a ligand to direct substitution *trans* to itself in a square planar complex, and is critical to directing the coordination site of an incoming ligand to a platinum(II) metal centre [29].

The *trans*-symmetric nature of the target N_3-TriplatinNC complex permits multiple possible synthetic routes for its construction, however, the synthetic route designed in Fig. 1D appears most efficient as it avoids synthetic obstacles whereby: (i) uncoordinated (dangling) amine groups deactivate platinum(II) centres due to the formation of chelates; (ii) excessive deprotection steps limit the overall yield; (iii) polymerization side reactions occur; and (iv) sensitivity to light or heat hamper synthesis (Supplementary information). This route enabled the synthesis of the target asymmetric complex containing a dangling azide linker, in moderate yield, in stepwise fashion using transplatin (*trans*- $[PtCl_2(NH_3)_2]$) as the starting material. The synthetic method involves successive activations using silver nitrate to remove the labile chlorido ligands asymmetrically, allowing for stepwise ligand coordinations. Following (ii) in Fig. 1D, the di-platinum intermediate is singly activated allowing the co-ordination of the azide-containing mono-platinum complex obtained in step (i) while avoiding the use of bases. This also leaves a single labile chlorido ligand, allowing further activation in (iv) to facilitate the asymmetric synthesis of N_3-TriplatinNC. Details of alternate synthetic routes that were attempted are included in the Supplementary Section 1.3. All complexes were characterized by ^{1}H NMR, ^{13}C NMR, DEPT, ^{195}Pt NMR, FT-IR, elemental analysis, and HPLC (Supplementary Fig. S1-S8). Mass analysis of the target complex proved difficult to obtain due to the gas phase stability of the complex; however, fragments containing three platinum centres coordinated to the dangling azide ligand were observed (Supplementary Figs S9 and S10).

Nucleic acid interactions

To probe the DNA targeting activity of N_3-TriplatinNC, a variety of techniques including competitive displacement, fluorescence quenching, thermal melting, microscale thermophoresis (MST), and single DNA molecule imaging were employed. These experiments were designed to understand the azide-PPC DNA interaction, as well as to establish if the azide handle preserves DNA recognition and downstream biological activity relative to the parent TriplatinNC complex.

We monitored the bulk solution DNA binding properties of the azide-appended and parent TriplatinNC complexes (Fig. 2A). Here, ethidium bromide competitive displacement assays were performed to determine the binding affinity (K_{app}). Once DNA is exposed to ethidium bromide and all possible bind-

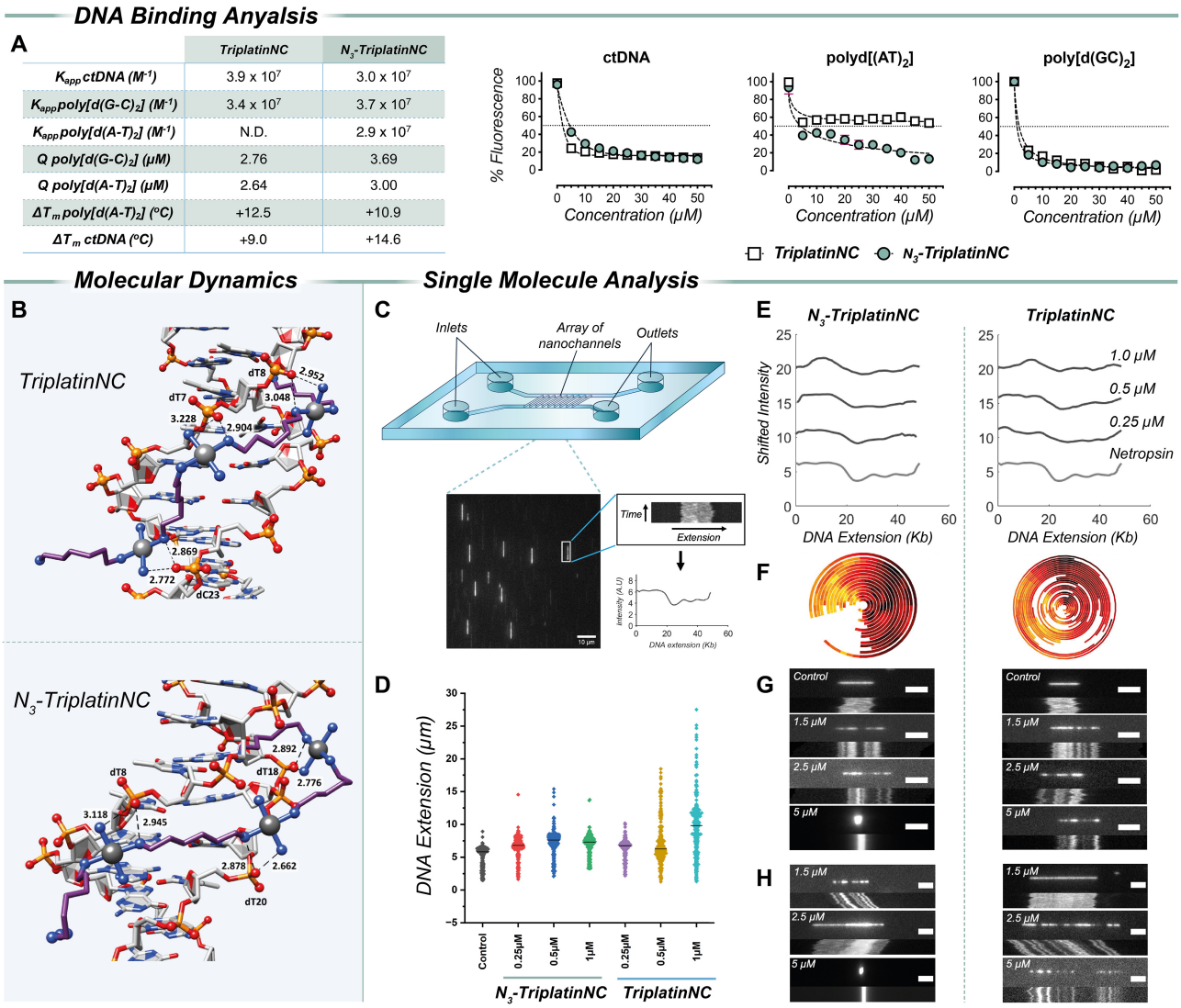

Figure 2. (**A**) Summary table of binding data for TriplatinNC and N_3-TriplatinNC along with ethidium bromide displacement assay results for calf thymus, poly A-T and poly G-C DNA. (**B**) Representative molecular dynamics (MD) structures of TriplatinNC and N_3-TriplatinNC bound to the Dickerson–Drew dodecamer (DDD), obtained via cluster analysis. Both PPCs exhibit similar binding modes, including phosphate clamp interactions with OP1 oxygen atoms and groove-spanning. Importantly, the azide handle in N_3-TriplatinNC positions itself away from the double-helix, enabling post-binding CuAAC. (**C**) Schematic of the nanofluidic experimental setup. The nanofluidic device with loading reservoirs connecting the two microchannels and the nanochannels (500 μm length, 150 nm width and 100 nm height) spanning between the two microchannels. A representative fluorescence microscopy image is shown from which kymographs can be extracted for each DNA molecule. Kymographs from tens of DNA molecules are used to obtain an intensity versus extension plot, showing the extension and the intensity profile that reflects the underlying DNA sequence. (**D**) Scatter plot showing DNA extensions for λ-DNA molecules (control) λ-DNA molecules exposed to 0.25, 0.5, and 1 μM concentrations of N_3-TriplatinNC and TriplatinNC. The black lines represent the median DNA extension. (**E**) Average intensity profile of λ-DNA labelled with YOYO dye and 0.25, 0.5, and 1 μM N_3-TriplatinNC (left) and TriplatinNC (right) compared with λ-DNA labelled with netropsin-YOYO one-step competitive binding (grey). (**F**) Representative concentric plots from tens of DNA molecules to reveal if the N_3-TriplatinNC/TriplatinNC – YOYO binding creates highly similar intensity patterns (N_3-TriplatinNC) or random intensity patterns (TriplatinNC) across different DNA molecules. The scale bar is 5 μm. (**G**) Representative image and kymograph for control (untreated) DNA along with 1.5, 2.5, and 5 μM N_3-TriplatinNC (left) and TriplatinNC (right). (**H**) Representative images and kymographs displaying clustered and branched DNA molecules observed in experiments with N_3-TriplatinNC and DNA concatemers with bright-dark intensity patterns observed in experiments with TriplatinNC. The scale bar is 5 μm.

ing sites are occupied, a nonfluorescent DNA binder is titrated into the reaction and the K_{app} is determined by the concentration of competitor required to reduce fluorescence intensity by 50%. Overall, the binding of both complexes is similar and the azide group does not impede DNA recognition. However, a notable difference between N_3-TriplatinNC and TriplatinNC stems from analysis with poly[d(A-T)$_2$] (inset plot Fig. 2A), a synthetic DNA co-polymer made up entirely of adenine and thymine bases. Unlike TriplatinNC, which has limited binding to this co-polymer [11], N_3-TriplatinNC appreciably binds in line with activity observed toward calf thymus DNA (ctDNA) and poly[d(G-C)$_2$] substrates. Additional experiments measuring fluorescence quenching (Q), a method conducted with limited bound ethidium bromide that aids in discovering preferential DNA binding sites bases, and thermal melting (ΔT_m) analysis, a method measuring the relative stabilization a drug molecule imparts to the DNA duplex as it thermally denatures, confirmed both PPCs are high

affinity DNA binders (Supplementary Figs S11 and S12, and Supplementary Tables S1 and S2).

To delineate the DNA-binding mode of N_3-TriplatinNC further, MD simulations were undertaken using TriplatinNC as a comparison (Fig. 2B, Supplementary Figs S17–S24, and Supplementary Table S3). Here, the B-DNA dodecamer (PDB 2DYW) was selected as a model and the reported X-ray structure was used to prepare the starting geometry for MD simulations on both platinum complexes over 200 ns. In this timeframe, the simulated interaction of B-DNA with N_3-TriplatinNC and TriplatinNC did not significantly influence the length of the DNA, nor did it induce significant distortion to the DNA structure. In the first 100 ns, neither complex adopted a stable binding position, displaying interactions with both the major and minor grooves of the DNA. However, after 100 ns, a clear dominance of interactions with the minor groove emerged with all selected frames converging to this stable binding position. Significantly, the azide group of N_3-TriplatinNC often remained at a considerable distance from the DNA backbone, suggesting intracellular click labelling should remain viable after DNA recognition (Fig. 2B). The binding mode obtained by MD can be compared to that described in the crystal structure of TriplatinNC bound to the Dickerson–Drew dodecamer [13], where backbone tracking and groove spanning interactions were first observed. Throughout the MD simulations performed in this study, phosphate clamp interactions were observed with OP1 oxygens of C23, T7, and T8. These results validate the quality of the model and can be extrapolated to the newly designed N_3-TriplatinNC.

The interaction of both PPCs with linear DNA was then investigated by confining single λ-DNA molecules (48 502 bp) in nanofluidic channels (Fig. 2C; see the 'Materials and methods' section) [23]. The experiments were conducted using N_3-TriplatinNC and TriplatinNC at concentrations ranging from 0.25 μM to 5 μM, while maintaining a constant λ-DNA concentration of 4.8 μM base-pairs. The ratio of PCCs to DNA base-pairs was thus varied from ∼1:20 to ∼1:1. Results for concentrations up to 1 μM N_3-TriplatinNC/TriplatinNC are summarized in a scatter plot (Fig. 2D) showing the distribution of DNA extension in the presence of N_3-TriplatinNC or TriplatinNC (n = ∼225 DNA molecules for each concentration). There is a high probability region with tails of varying lengths on both sides. The tail at short extensions is from fragmentation of λ-DNA molecules, formed due to shearing of DNA during sample preparation. For N_3-TriplatinNC, we observe a concentration dependent increase in average DNA extension, the median DNA extension for the control sample is 5.1 μm and this increases from 6.4 μm (0.25 μM exposure) up to 7.3 μm (0.5 μM) and 6.9 μm (1 μM). For TriplatinNC, the result at 0.25 μM is very similar to N_3-TriplatinNC; however, at 0.5 μM, a significant fraction of much longer DNA molecules, with extensions of up to 20 μm, were observed (Supplementary Fig. S13–S16). This is not due to an increase in the extension of individual DNA molecules, but rather the formation of concatemers arising from adjoining trains of DNA molecules [30]. Linearized λ-DNA has complimentary 12-base overhangs at the ends and TriplatinNC facilitates hybridization of these overhangs to form DNA chains, a phenomenon that is even more pronounced at 1 μM, where concatemers of at least four λ-DNA molecules were observed.

To visualize DNA in the nanochannels, we used the bis-intercalating dye YOYO-1. From the images of the confined DNA, it is clear N_3-TriplatinNC and TriplatinNC compete with YOYO-1. To analyse this in more detail, we generated average intensity profiles of N_3-TriplatinNC and TriplatinNC concentrations up to 1 μM. Further, these intensity profiles were compared with the average intensity profile of λ-DNA molecules with YOYO-1 and netropsin bound (Fig. 2E). Netropsin binds highly specifically to AT-rich regions of DNA and blocks YOYO-1 from binding. Since one half of λ-DNA is AT-rich and the other is GC-rich, an intensity profile along the λ-DNA has a characteristic pattern, with one bright, GC-rich half and one dark, AT-rich half that reflects the underlying DNA sequence [23–25]. Although not as marked as the YOYO-netropsin intensity profiles, one half of DNA had higher YOYO-1 emission intensity for the majority of DNA molecules exposed to either N_3-TriplatinNC or TriplatinNC bound. This indicates that there is a preferential binding of the ligands to AT-rich regions. When these intensity profiles are aligned into a concentric plot, similar barcodes render a plot with the DNA ends aligned at the same location [31]. However, intensity profiles from dissimilar patterns render a concentric plot with random DNA ends. For N_3-TriplatinNC, DNA molecules in the concentric plots were well aligned, showing N_3-TriplatinNC binding is highly specific most likely due to a consistent groove spanning binding motif. In contrast, TriplatinNC binding is more random and thus the intensity profile varies between DNA molecules (Fig. 2F). This result reflects a combination of binding modes at play and is consistent with the earlier DNA extension experiments (Fig. 2D).

To understand the binding properties at higher concentrations, we next studied images of both complexes bound to λ-DNA up to 5 μM (Fig. 2G and Supplementary Figs S13 and S14). N_3-TriplatinNC showed bright-dark patterns along the DNA molecules above 1 μM. Interestingly, exposure to 2 μM and 2.5 μM identified high intensity regions along the stretched DNA molecules, possibly from localized DNA compaction by N_3-TriplatinNC. At 5 μM N_3-TriplatinNC, complete DNA condensation occurs, and most DNA molecules were trapped at the loading reservoirs near the microchannel entrance. The kymograph for the 5 μM N_3-TriplatinNC concentration in Fig. 2E was obtained from a DNA molecule that was nonspecifically adsorbed to the microchannels, as we could not see any DNA molecules entering the nanochannels. For TriplatinNC, the main difference at the lower drug exposure was the formation of bright and dark patches of varying intensity along the stretched DNA molecules, a phenomenon that was even more pronounced when the concentration was increased (Fig. 2G and Supplementary Fig. S15 and S16). In the presence of 5 μM TriplatinNC, the binding of YOYO-1 was largely outcompeted rendering DNA-molecules difficult to observe. Finally, at concentrations above 1.5 μM of N_3-TriplatinNC, there were some instances where more than one DNA molecule was clustered together forming branched chains of DNA, squeezed into the nanochannels, showing very bright patches along the DNA molecule (Fig. 2H). We speculate that this phenomenon is caused by N_3-TriplatinNC bridging at least two DNA molecules. For TriplatinNC, concentrations > 1.5 μM reliably produce concatemers with bright-dark intensity patterns (Fig. 2H).

Microscale thermophoresis

To probe the binding differences of N_3-TriplatinNC to AT-rich and GC-rich DNA and to elaborate on the findings of

the single molecule analysis, assays with well-defined hairpin sequences were designed using MST, a relatively new technique that quantifies molecular interactions based on changes in thermophoretic mobility. In this assay, a solution containing a fluorescently labelled biomolecule (in our case, DNA hairpins) is loaded onto a capillary [32, 33]. A focused IR-Laser is used to locally heat a defined sample volume, while the thermophoresis of fluorescent molecules through the temperature gradient is detected.

The mobility of the biomolecule is controlled by structural factors such as charge density, size, and entropy of the hydration shell, allowing the detection of changes in the migration behaviour upon binding to a ligand (in our case, the PPCs). Using A-T rich and G-C rich hairpins labelled with the Cy5 fluorophore, normalized fluorescence changes ($\%F_{norm}$) obtained over a concentration gradient were used to determine the DNA binding properties.

The two curves indicate the MST trace—the change measured in thermophoresis over increasing concentrations of compound—and the initial fluorescence, which is the direct change in fluorescent signal. F-D6aH (an AT-rich sequence containing the TATA domain) and F-TP (a GC-rich sequence) hairpins were designed and labelled with Cy5 at the 5′ terminus (Fig. 3). Experiments were performed using 0.075 μM–10 μM of N_3-TriplainNC together with 0.1 μM of DNA (see Supplementary Information Section 2.6 for full method). The results show an increase in binding affinity correlated with a decrease in initial fluorescence as the complex concentration increases. This decrease is associated with the binding of the complex together with condensation and aggregation, a phenomenon previously observed with TriplatinNC and longer DNA polymers [12,34]. With the GC-rich hairpin (F-TP), N_3-TriplatinNC reported an IC_{50} of 1.9 μM and an EC_{50} of 0.6 μM, while for the AT-rich sequence (F-D6aH), respective values of 3.7 μM and 0.7 μM were obtained. Interestingly, IC_{50} values seem to be impacted by aggregation effects above 2 μM on F-TP that alter the MST trace results, visible by a jump in MST signal seen between capillaries (Supplementary Figs S25 and S26). The EC_{50} values are, however, relatively unaffected as changes in fluorescence occur before condensation takes effect. This suggests that the AT-rich sequence accommodates more compound before fluorescence is inhibited, while for the GC-rich hairpin, lower concentrations of N_3-TriplainNC are required to condense DNA. This effect appears linked to the binding site size with fewer interactions permitted on GC-rich sequences due to the preferred backbone tracking mode where the PPC is bound in an extended form.

Topoisomerase IA relaxation assay and in-liquid AFM analysis

To further investigate the condensation/aggregation properties of N_3-TriplatinNC, turbidity experiments with ctDNA were performed at 350 nm (a wavelength where insoluble DNA aggregates generated by condensation can be measured) and revealed higher condensation effects (as observed by the maximum A350) than the parent TriplatinNC (Supplementary Fig. S27). Next, to understand the downstream biological impact associated with DNA condensation [35], topoisomerase IA relaxation assay was designed and monitored using agarose gel electrophoresis for the resolution of topoisomers in tandem with in-liquid AFM imaging (Fig. 4). Topoisomerase (Topo) enzymes play a vital role in maintaining cellular function by relieving topological constraints generated during processes such as gene transcription, DNA replication, recombination, and repair. Inhibition by alteration of DNA topology or poisoning of Topo enzymes leads to alterations in resulting DNA supercoiling which has been successfully targeted for cancer treatment [36]. We used Topo IA, which is inhibited by TriplatinNC binding to plasmid DNA [34] to evaluate whether the azide modification in N_3-TriplatinNC alters the enzyme's recognition of PPC-bound DNA. In the case of TriplatinNC, and we hypothesize N_3-TriplatinNC, this occurs through the overwinding or condensation of DNA by the drug, rendering the supercoiled DNA unrecognizable by Topo IA.

First, this assay demonstrated that N_3-TriplatinNC retained the ability to inhibit the Topo IA-mediated plasmid DNA relaxation found for the parent TriplatinNC (Fig. 4A and D). The formation of condensates was observed by the trapping of DNA in the loading wells, which is visible, albeit to different extents, for both compounds. Interestingly, condensation onsets earlier with the azide appended complex (lane 4; 0.5 μM N_3-TriplatinNC) and precedes PPC-mediated positive supercoiling (lane 7; 2.5 μM N_3-TriplatinNC). This positive supercoiling was confirmed by two-dimensional gel electrophoresis using chloroquine (a known positive overwinding agent) as a control (Supplementary Fig. S29). Here it was observed that N_3-TriplatinNC matches the migration pattern of chloroquine and positively overwinds the DNA. Further discussion can be found in the Supplementary Information (Section 2.9). Topo IA acts only on negatively supercoiled DNA as evidenced by the generation of topoisomer bands in lanes 2–6 and 19. Complete enzyme inhibition is observed in lane 7 (2.5 μM N_3-TriplatinNC) where a fraction of plasmid DNA is condensed in the loading well together with another fraction of supercoiled DNA which, due to the lack of observable topoisomers, appears to have undergone a transition to the positive state. Chemically induced positive supercoiling has, to this point, only been observed by classical DNA intercalators that overwind negatively supercoiled DNA and thereby inhibit Topo IA recognition [37]. A similar profile was observed in reactions with TriplatinNC (Fig. 4D) where positive supercoiling is observed (lane 8; 5 μM TriplatinNC) prior to the onset of total aggregation (lanes 10–18). Importantly, Topo IA recognition is inhibited at a lower concentration of N_3-TriplatinNC than TriplatinNC. N_3-TriplatinNC initiates Topo IA inhibition and leads to complete inhibition at lower concentrations when compared to TriplatinNC. This observation, along with our findings by single molecule nanofluidics experiments and MST, are likely due to the higher occupancy of N_3-TriplatinNC on a given DNA target and also due to its intrinsic, differential affinity towards binding AT-rich regions when compared to TriplatinNC.

Finally, to better understand the key events during PPC-induced pUC19 unwinding, we derived a Topo IA relaxation assay coupled with high resolution in-liquid AFM (Fig. 4B, E). For both compounds, four conditions from the gel electrophoresis experiment were picked for imaging: a sample prior to the onset of compound-induced Topo IA inhibition (light pink); a sample with a low degree of Topo IA inhibition and a low level of DNA condensation (pink); complete Topo IA inhibition resulting from DNA positive supercoiling (dark pink); and a sample with extensive DNA condensation (purple). For the AFM images, quantification of the Topo IA inhibition (i.e. molecular compaction) and condensation

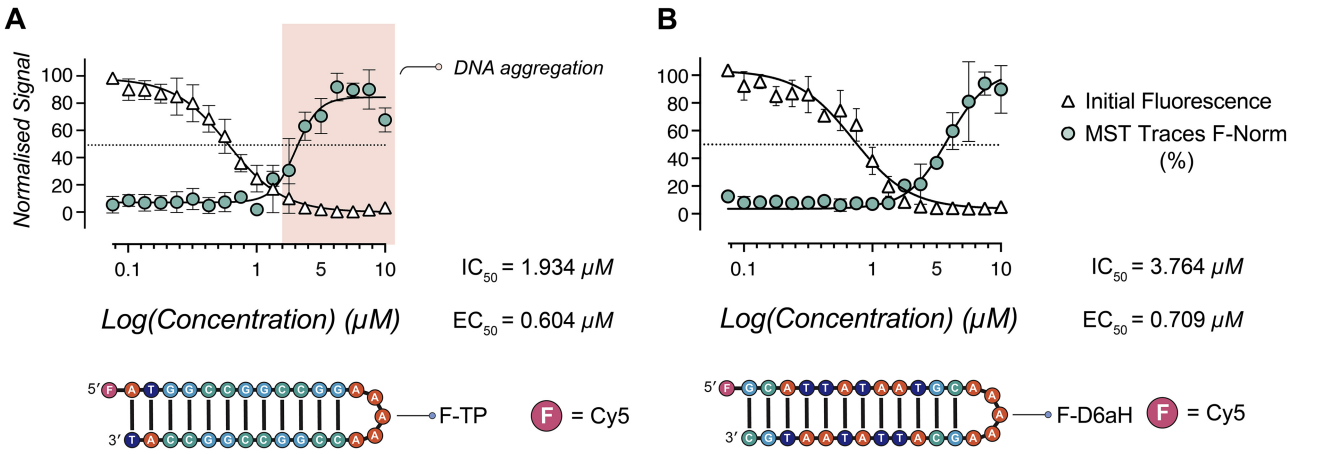

Figure 3. MST results for N_3-TriplatinNC. (**A**) MST results showing normalized MST signal and initial fluorescence using the F-TP (GC-rich) hairpin. (**B**) Normalized MST signal and initial fluorescence using the F-D6aH (AT-rich) ranging from 0.075 μM to 10 μM of N_3-TriplatinNC DNA hairpins tagged with the Cy5 fluorophore.

(i.e. intermolecular aggregation) was performed. Automated analysis of all AFM images was carried out using TopoStats [27] to calculate the smallest bounding area of DNA complexes (Fig. 4C and F). pUC19 treated with low concentrations of PPCs (Fig. 4B + E; light pink) appear very similar to the control (Fig. 4B + E; grey), which is reflected in a similar value for the smallest bounding area of the molecules (Fig. 4C + F). At the point of Topo IA inhibition (Fig. 4B; pink) the pUC19 molecules are more compacted (Fig. 4C) consistent with the onset of increased supercoiling observed by gel electrophoresis. At the point where total Topo IA inhibition is achieved by positive DNA supercoiling, extensive DNA aggregation is observed (Fig. 4B + E; dark pink). This is confirmed by the quantitative analysis which shows an increase in the number of large bounding area complexes (Fig. 4C + F).

This demonstrates that upon aggregate formation, the Topo IA is unable to recognize and unwind the plasmid DNA substrate. At high concentrations of the PPCs, after extensive aggregation, we measure a reduction in the molecule size (Fig. 4C + F) which is believed to be a result of very large complexes that were not detected in the image areas (Fig. 4E; purple). This is reflected by the lower number of DNA molecules (N) for this measurement. Overall, the qualitative analysis by visual inspection and the quantitative analysis using TopoStats demonstrate that the incorporation of the reactive azide handle in N_3-TriplatinNC results in DNA binding similar to that of the parent compound, TriplatinNC, with consequent inhibition of Topo I-mediated plasmid DNA relaxation. This inhibition occurs through the same DNA topological intermediates, as imaged using high-resolution in-liquid AFM imaging.

We captured the dynamic behaviour of TriplatinNC-induced pUC19 condensation in-liquid (Supplementary Fig. S28). In this experiment, intramolecular condensation was observed in consecutive AFM images acquired on the same pUC19 molecule. In the initial stage (blue panel), the pUC19 molecule is already bound by TriplatinNC molecules. As time passes, we observed a marked change in topology, with the formation of a knot-like region in the bottom right portion of the plasmid (purple panel). Importantly, the initial topology of the plasmid molecule that underwent intramolecular condensation is markedly different and appears more "rigid" in comparison to the untreated pUC19 (black panel). The condensation/aggregation observed in the topoisomerase IA relaxation gel and AFM experiments is also apparent in the MST suggesting N_3-TriplatinNC is a powerful condensing agent, even more so than TriplatinNC. The comparable condensing effects of N_3-TriplatinNC and TriplatinNC are also supported by MD data (Supplementary Section 2.5).

Intracellular tracking of N_3-TriplatinNC in MDA-MB-231 TNBC

N_3-TriplatinNC was bioorthogonally coupled with a fluorescent label by copper(I) catalysed azide-alkyne cycloaddition (CuAAC) to investigate selective localization in TNBC cells (Fig. 5). MDA-MB-231 cells were exposed to 10 μM N_3-TriplatinNC for 24 and 48 h prior to fixation. Treated cells were then labelled using click chemistry where a 1:1 ratio of alkyne fluorophore to N_3-TriplatinNC complex (pre-exposed to the cell line) were combined in the presence of $CuSO_4$ with added ascorbate. Distinct organelles, such as nuclei and mitochondria, were counterstained to distinguish the overall cell structure and compartmental accumulation of the trinuclear complex. Nonspecific uptake of the unclicked dye was not observed in nontreated control cells as no fluorescence was detected (Fig. 5). There was little or no overlap of fluorophore-labelled N_3-TriplatinNC with nuclear chromatin and mitochondrial structures. Predominant and uniform accumulation was shown in nucleolar compartments, the only intranuclear component of the nucleus in eukaryotic cells, suggesting localization in the region responsible for ribosomal biogenesis.

We validated this observation through immunofluorescent staining of NPM, also known as B23, a nucleolar phosphoprotein involved in diverse cellular processes. It shuttles between the nucleus and cytoplasm but predominately resides in the perimeter of the nucleoli. NPM was detected using a monoclonal mouse anti-NPM antibody as the primary antibody which was subsequently stained with a goat antimouse IgG secondary antibody fragment conjugated to a complimentary fluorophore. The observed nucleolar localization properties demonstrate that the azide complex retains intracellular behaviour in line with the expected activity of this PPC. Thus,

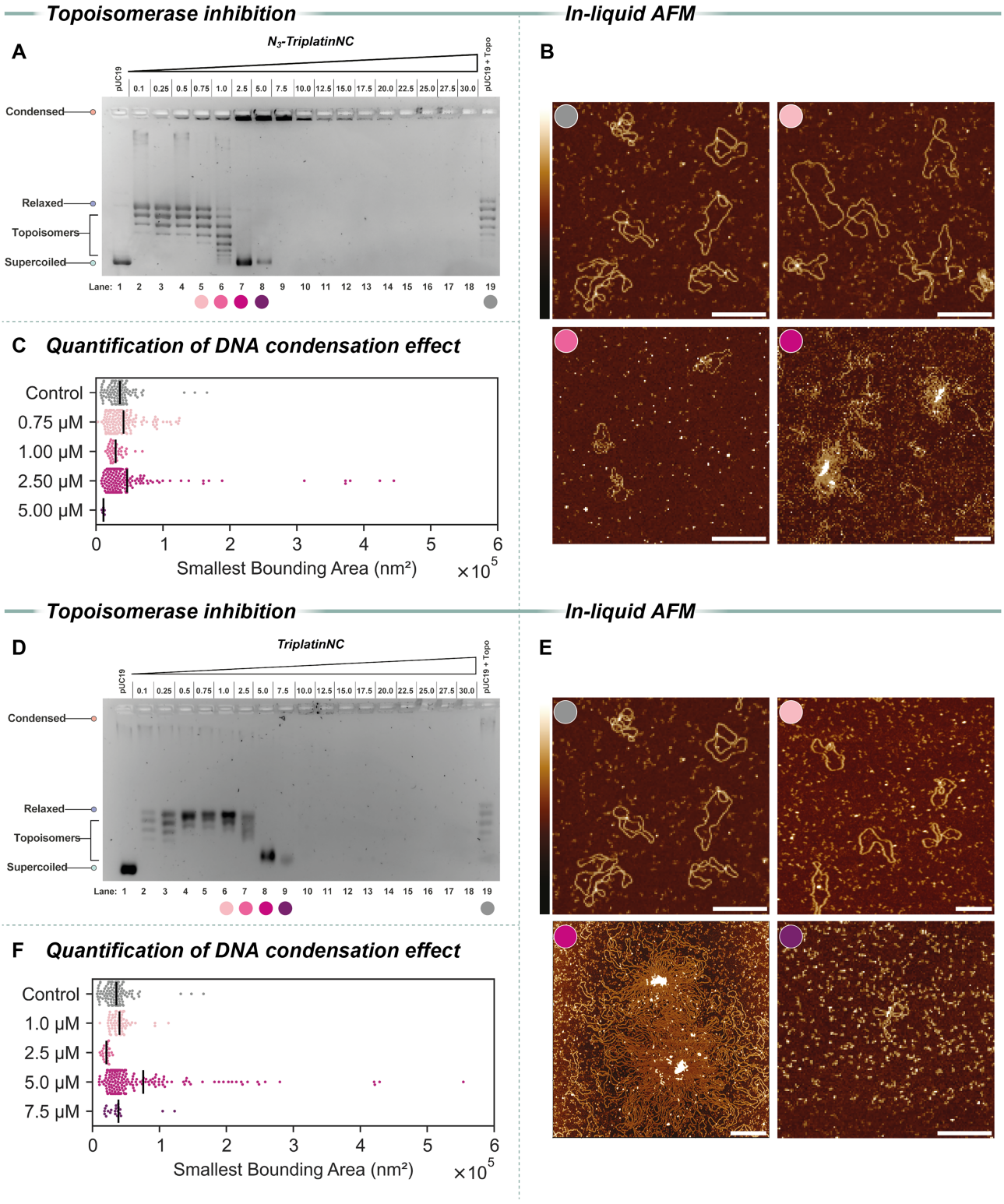

Figure 4. (**A, D**) Topoisomerase IA relaxtion assay monitored by agarose gel electrophoresis assay as consequence of pre-exposure of pUC19 (400 ng) to either N_3-TriplatinNC or TriplatinNC at the indicated concentration, followed by addition of the enzyme. (**B, E**) The inhibition of DNA unwinding was probed by high resolution in-liquid AFM colour-coded to specific concentrations used in electrophoretic experiments performed in A and D: untreated control (grey), 0.75 μM N_3-TriplatinNC or 1.0 μM TriplatinNC (light pink), 1 μM N_3-TriplatinNC (pink), 2.50 μM N_3-TriplatinNC or 5.0 μM TriplatinNC (dark pink), and 7.5 μM TriplatinNC (purple). Scale bars: 250 nm, Z-scale: −3 to 4 nm. (**C, F**) Quantitative analysis of DNA condensation was performed by measuring the smallest bounding area of DNA complexes observed in AFM images using TopoStats [28]. N values are as follows – Control: 113, N_3-TriplatinNC 0.75 μM: 143, 1.0 μM: 42, 2.5 μM: 211, 5.0 μM: 5, TriplatinNC 1.0 μM: 72, 2.5 μM: 25, 5.0 μM: 207, 7.5 μM: 21.

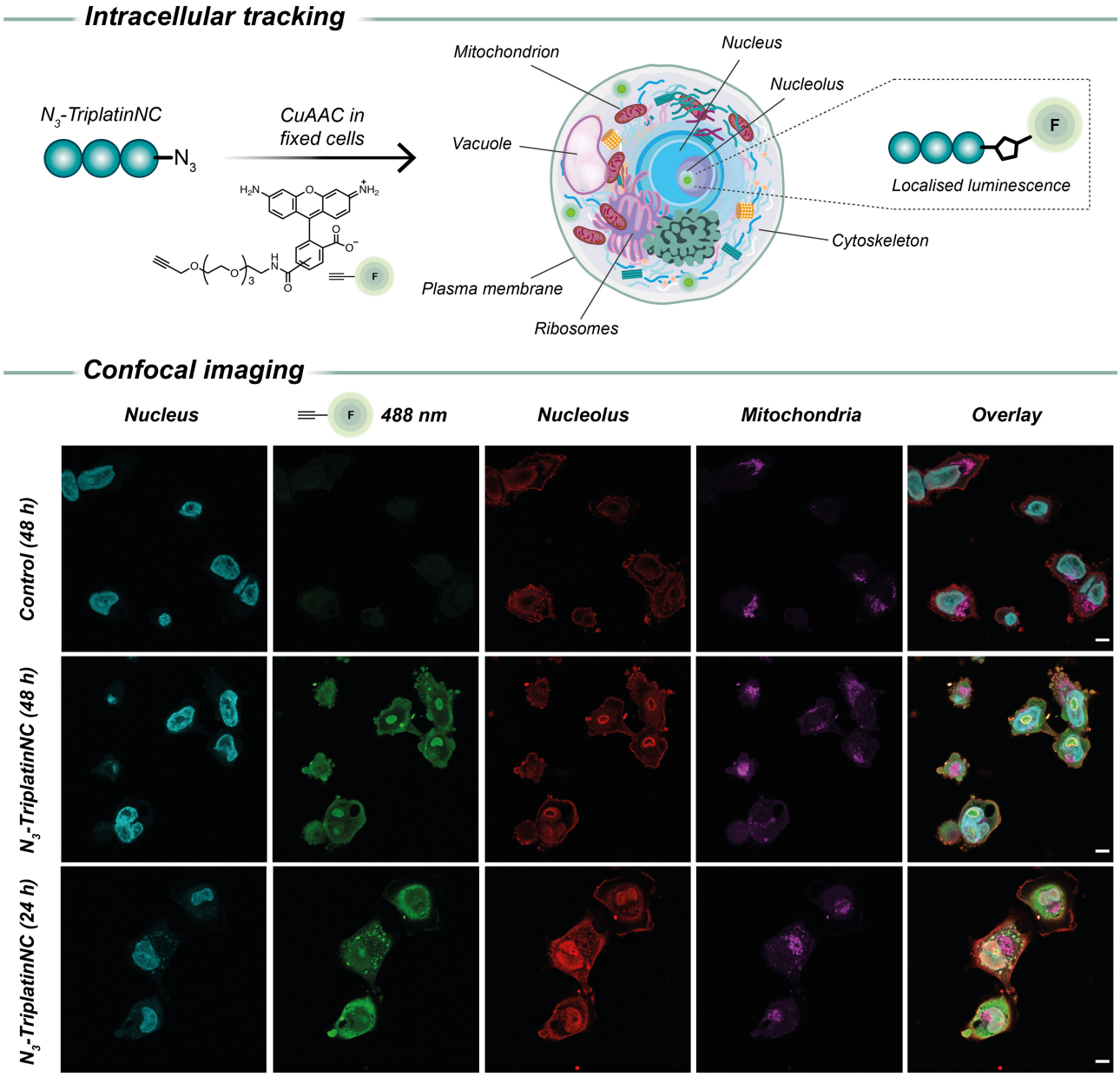

Figure 5. Intracellular fluorescent labelling of N_3-TriplatinNC through CuAAC chemistry to examine cellular uptake and localization. Confocal microscope images below on 63× oil immersion lens of fixed MDA-MB-231 cells exposed to 5 and 10 μM for 48 and 24 h, respectively, and clicked to alkyne 488 dye (green). Nuclei were stained with NucBlue Fixed (blue), mitochondria were stained with MitoTracker Deep Red (magenta) and nucleoli were visualized by immunofluorescent staining of NPM (red). Scale bars indicate 10 μm (overlay, bottom right corner).

N_3-TriplatinNC exhibits similar localization to TriplatinNC, which is trafficked to the same subcellular compartment, resulting in apoptosis after interfering with the G1 stage of mitosis [14].

This is not surprising given the similarity to the nonfunctionalized parent compound, TriplatinNC, throughout the experiments presented in this body of work. In samples presented over 48 h, morphological changes characteristic of apoptotic cell death are indicated with the formation of apoptotic bodies and blebbing caused by membrane degradation in which high concentrations of the click-labelled complex was observed. Evidence of distinct voids, most likely cytosolic vacuoles, suggests that selective organelle accumulation is facilitated by the high cationic complex charge of N_3-TriplatinNC.

In vitro cytotoxic analysis and NCI-60 results

Since N_3-TriplatinNC maintained broad DNA recognition and cellular trafficking properties analogous to TriplatinNC, we next probed the anticancer properties of this new labelled complex. Recalcitrant breast cancer cell lines MCF-7, T-47D, MDA-MB-231, MDA-MB-468 were selected for cytotoxic analysis, with T-47D being a ductal carcinoma while all other cancer lines are adenocarcinomas. Each line is further categorized into molecular sub-types based on expression levels, grade, and prognosis (Supplementary Table S4). N_3-TriplatinNC exhibits low micromolar antiproliferative activity across all cell lines tested at both 24 and 48 h (Fig. 6A). Cisplatin displayed effective antiproliferative activity in MDA-MB-468 cells with an IC_{50} of 2.9 μM after 48 h in agree-

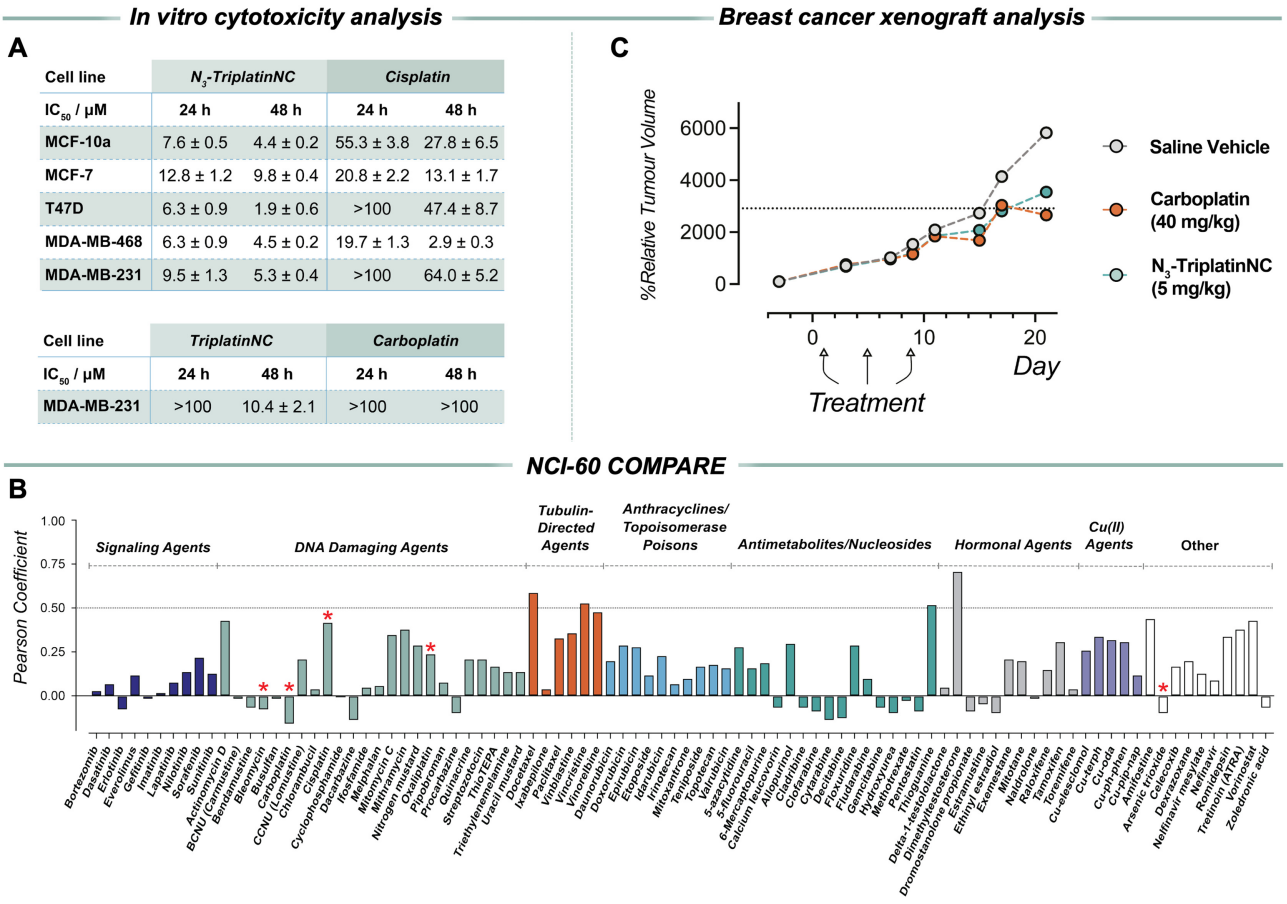

Cell line	N_3-TriplatinNC		Cisplatin	
IC_{50} / μM	24 h	48 h	24 h	48 h
MCF-10a	7.6 ± 0.5	4.4 ± 0.2	55.3 ± 3.8	27.8 ± 6.5
MCF-7	12.8 ± 1.2	9.8 ± 0.4	20.8 ± 2.2	13.1 ± 1.7
T47D	6.3 ± 0.9	1.9 ± 0.6	>100	47.4 ± 8.7
MDA-MB-468	6.3 ± 0.9	4.5 ± 0.2	19.7 ± 1.3	2.9 ± 0.3
MDA-MB-231	9.5 ± 1.3	5.3 ± 0.4	>100	64.0 ± 5.2

Cell line	TriplatinNC		Carboplatin	
IC_{50} / μM	24 h	48 h	24 h	48 h
MDA-MB-231	>100	10.4 ± 2.1	>100	>100

Figure 6. (**A**) *In vitro* cytotoxicity data for N_3-TriplatinNC, TriplatinNC, cisplatin, and carboplatin toward selected breast cancer cell types. (**B**) NCI-60 LC_{50} comparing N_3-TriplatinNC versus studied anticancer agents (note: metallodrugs cisplatin, carboplatin, oxaliplatin, bleomycin and arsenic trioxide are marked with an asterisk). (**C**) Relative tumour volume in mice bearing MDA-MB-231 breast cancer xenografts, highlighting N_3-TriplatinNC's lower dose (5 mg/kg) to achieve similar effect to carboplatin (40 mg/kg).

ment with work from Predarska *et al.* [38]. However, a significant antiproliferative difference between N_3-TriplatinNC and cisplatin was observed in MDA-MB-231 cells, with respective IC_{50} values of 5.3 and 64.0 μM being recorded. Further analysis using MDA-MB-231 cells (Fig. 6A) revealed that N_3-TriplatinNC exhibits significantly higher 24 h cytotoxicity and moderately enhanced activity at 48 h compared to the parent, nonazide, compound. Notably, N_3-TriplatinNC was also considerably more effective than a carboplatin control. Overall, these findings indicate that the azide-modified compound possesses low micromolar activity against TNBC.

N_3-TriplatinNC was submitted to the US NCI DTP 60 human cancer cell line screen. The cytotoxic or lethal effects (LC_{50}) and growth inhibitory properties (50% growth inhibition, GI_{50} and TGI) were identified using a five-dose exposure level and are shown in Supplementary Table S5. The corresponding heat map (Supplementary Fig. S30) show the most sensitive cell lines in the 0.1–15 μM exposure range were COLO 205 (colon) and SK-MEL-5 (melanoma). Meanwhile, at 15–30 μM exposure, increased activity towards HCC2998 and KM12 (colon), SK-MEL-2 (melanoma), and TK-10 (renal) were identified. Activity profiles were then analysed using the COMPARE algorithm which compared N_3-TriplatinNC against established marketed drugs, mechanistic and standard agent datasets to correlate plausible modes of action (Fig. 6 and Supplementary Table S6). The comparison results are represented as Pearson's correlation coefficients (r) ranging from −1 to +1, with values closer to +1 indicating a high degree of similarity (in terms of cytotoxic profile) with the known anticancer agents. While dimethyltestosterone, thioguanine, vincristine, and docetaxel had the highest correlations (>0.5), typical metal-based chemotherapeutics such as bleomycin, cisplatin, carboplatin, oxaliplatin, and arsenic trioxide (Fig. 6B) all show limited or negative correlation to N_3-TriplatinNC. This observation is consistent with the previously established unique binding mode of the parent TriplatinNC.

In-vivo cytotoxicity studies of N_3-TriplatinNC in mice bearing MDA-MB-231 xenografts

Following the establishment of *in vitro* cytotoxicity of N_3-TriplatinNC towards the TNBC cell line MDA-MB-231, *in vivo* cytotoxicity studies were conducted on mice bearing MDA-MB-231 breast cancer xenografts. The cell line is particularly invasive when animal models are implanted to produce xenografts as the tumours undergo metastases that spread to the lymph nodes [39]. *In vivo* studies were conducted using NCG mice at The Department of Pathology, The Massey Centre, VCU. Analysis of primary tumour growth after 20 days showed close to 50% regression in relative tumour volume. IVIS luminescent detection of cancer cells similarly corrobo-

rate a reduction in tumour size in drug-treated mice compared to saline controls (Supplementary Fig. S31).

Significantly, the trinuclear complex showed comparable results at an exposure eight-times lower (5 mg/kg) than the carboplatin clinical standard used (40 mg/kg). Thus, N_3-TriplatinNC shows promise as a trackable PPC for treating TNBCs that are chemoresistant to standard platinum therapies.

Conclusion

The last platinum(II)-based drug to receive worldwide clinical approval was oxaliplatin in 2002. This compound, along with carboplatin and cisplatin, have dramatically improved mortality rates and revolutionized cancer treatment. However, all three compounds share a common DNA crosslinking mode of action and are therefore limited by intrinsic resistance factors that are particularly prevalent in recalcitrant, or untreatable, tumours, such as TNBC. Formally substitution-inert PPCs represent a unique sub-class of platinum-based anticancer agents as the biological consequences of their action are achieved in the absence of covalent binding; a feature which has been considered critical for biological activity and which further distinguishes the NC (noncovalent) class from cisplatin and congeners. The biological consequences include efficient nucleic acid condensation, good *in vivo* antitumour activity and possible direct antimetastatic effects. In this work, we present a first-in-class approach to asymmetrically prepare N_3-TriplatinNC, an azide-functionalized polynuclear platinum(II) complex. Subsequent bioorthogonal click chemistry allows for its cellular trafficking and biodistribution properties to be studied in absence of any molecular modifications such as dye-labelling which may affect activity. The *in situ* labelling results for N_3-TriplatinNC presented here affirms this hypothesis and corroborates the nucleolar localization previously suggested by Peterson *et al*. for the unlabelled complex, TriplatinNC [14]. Through a series of carefully designed biophysical experiments comparing the properties of TriplatinNC to N_3-TriplatinNC—including single-molecule DNA imaging along with in-liquid AFM analysis—we demonstrate that the azide group does not diminish DNA binding activity but rather it retains analogous functionality and downstream biological consequences with improved AT sequence-specificity. A comparison of the single-molecule activity of this PPC with previously studied complexes cisplatin and oxaliplatin reveals a significant difference in the concentrations required to induce structural changes in DNA, with both mononuclear agents necessitating substantially higher concentrations compared to the PPC [40, 41]. The performance of N_3-TriplatinNC within the US NCI-60 human cancer cell line screen is unique in comparison to clinically approved metallodrugs bleomycin, cisplatin, carboplatin, oxaliplatin, and arsenic trioxide, which showed limited or negative correlation to this compound. N_3-TriplatinNC was then examined in mice bearing MDA-MB-231 (TNBC) xenografts and demonstrated comparable results at an exposure eight-times lower than the carboplatin clinical standard. Overall, the results suggest a deviation from the "classical DNA-centric" model of platinum drug development, which has been successful in producing cisplatin and second- and third-generation crosslinking analogues, to a new approach providing specificity and biological activity genuinely complementary to existing drugs. In this endeavour we suggest N_3-TriplatinNC as a powerful tool to probe the relationship of cellular trafficking to biological function.

Acknowledgements

We thank Dr Zara Molphy and Dr Simon Poole for assisting Dr Sineád O'Carroll and Mr Conor Newsome in their research activities. The nanofluidic devices used in this work were fabricated at Chalmers MyFab facility.

Author contributions: A.K. and N.P.F. acquired funding, conceptualized, performed writing of the original draft, and supervised the project. S.C. performed investigation, formal analysis, validation, and writing of the original draft. C.S., R.E.F.P., and C.N. performed investigation, formal analysis, validation, and writing of the original draft, review, and editing. B.S. performed formal analysis, methodology, validation and writing—review and editing. S.K., S.W., T.E.C., S.S., K.M., E.J.P., B.H., J.E.K., A.S., and V.M.K. performed investigation and formal analysis. A.L.B.P. and F.W. performed investigation, formal analysis, and supervision.

Supplementary data

Supplementary data is available at NAR online.

Conflict of interest

None declared.

Funding

A.K. acknowledges funding from Science Foundation Ireland (12/RC/2275_P2, 15/CDA/3648, and 13/RC/2073_2), the Irish Research Council (IR-CLA/2022/3815), the Novo Nordisk Foundation (NNF22OC0077099), and the European Union's Horizon 2020 research and innovation programme (Marie Skłodowska-Curie grant agreement no. 861381). R.E.F.d.P. acknowledges funding from the Government of Ireland Postdoctoral Fellowship program (GOIPD/2021/909). A.L.B.P. acknowledges funding from UKRI Future Leaders Fellowship MR/W00738X/1, the Henry Royce Institute for Advanced Materials, funded through EPSRC grants EP/R00661X/1, EP/S019367/1, EP/P02470X/1, and EP/P025285/1 and Xinyue Chen for Dimension FastScan access and support at Royce@Sheffield. F.W. acknowledges funding from the European Research Council (ERC consolidator, grant no. 866238), the Swedish Research Council (grant no. 2020-03400), the Swedish Cancer Foundation (grant no. 201 145 PjF) and the Swedish Child Cancer Foundation (grant no. PR2022-001). S.S. acknowledges funding from ICSC – Centro Nazionale di Ricerca in High Performance Computing, Big Data, and Quantum Computing, funded by the European Union – NextGenerationEU – PNRR, Missione 4, Componente 2, Investimento 1.4, as well as support from a 'Juan de la Cierva' fellowship (JDC2023–052228–I), funded by the Spanish Ministry of Science, Innovation and Universities, the National Research (MCIU/AEI/10.13039/501100011033), and the European Social Fund Plus (FSE+). Services and products in support of the research project were generated by the Virginia Commonwealth University Cancer Mouse Models Core Laboratory and/or the Tissue and Data Acquisition and Analysis Core Laboratory, supported, in part, with funding

to the Massey Cancer Center from NIH-NCI Cancer Center Support Grant P30 CA016059.

Data availability

The datasets generated during this study are available to view in the Supplementary Information. All code developed in this publication is publicly available on Github via TopoStats v2.3.0 https://github.com/AFM-SPM/TopoStats, and via Figshare with DOI: https://doi.org/10.15131/shef.data.22633528.v2.

References

1. Rosenberg B, Vancamp L, Krigas T. Inhibition of cell division in *Escherichia coli* by electrolysis products from a platinum electrode. *Nature* 1965;**205**:698–9. https://doi.org/10.1038/205698a0
2. Kelland L. The resurgence of platinum-based cancer chemotherapy. *Nat Rev Cancer* 2007;**7**:573–84. https://doi.org/10.1038/nrc2167
3. Galluzzi L, Vitale I, Michels J *et al.* Systems biology of cisplatin resistance: past, present and future. *Cell Death Dis* 2014;**5**:e1257. https://doi.org/10.1038/cddis.2013.428
4. Johnstone TC, Suntharalingam K, Lippard SJ. The next generation of platinum drugs: targeted Pt(II) agents, nanoparticle delivery, and Pt(IV) prodrugs. *Chem Rev* 2016;**116**:3436–86. https://doi.org/10.1021/acs.chemrev.5b00597
5. Hennessy J, McGorman B, Molphy Z *et al.* A click chemistry approach to targeted DNA crosslinking with cis-platinum(II)-modified triplex-forming oligonucleotides. *Angew Chem Int Ed* 2022;**61**:e202110455. https://doi.org/10.1002/anie.202110455
6. Manzotti C, Pratesi G, Menta E *et al.* BBR 3464: a novel triplatinum complex, exhibiting a preclinical profile of antitumor efficacy different from cisplatin. *Clin Cancer Res* 2000;**6**:2626–34.
7. Komeda S, Moulaei T, Woods KK *et al.* A third mode of DNA binding: phosphate clamps by a polynuclear platinum complex. *J Am Chem Soc* 2006;**128**:16092–103. https://doi.org/10.1021/ja062851y
8. Farrell NP. Multi-platinum anti-cancer agents. Substitution-inert compounds for tumor selectivity and new targets. *Chem Soc Rev* 2015;**44**:8773–85. https://doi.org/10.1039/C5CS00201J
9. Kellett A, Molphy Z, Slator C *et al.* Molecular methods for assessment of non-covalent metallodrug–DNA interactions. *Chem Soc Rev* 2019;**48**:971–88. https://doi.org/10.1039/C8CS00157J
10. Alt A, Lammens K, Chiocchini C *et al.* Bypass of DNA lesions generated during anticancer treatment with cisplatin by DNA polymerase η. *Science* 2007;**318**:967–70. https://doi.org/10.1126/science.1148242
11. Jodrell DI, Evans TRJ, Steward W *et al.* Phase II studies of BBR3464, a novel tri-nuclear platinum complex, in patients with gastric or gastro-oesophageal adenocarcinoma. *Eur J Cancer* 2004;**40**:1872–7. https://doi.org/10.1016/j.ejca.2004.04.032
12. Prisecaru A, Molphy Z, Kipping RG *et al.* The phosphate clamp: sequence selective nucleic acid binding profiles and conformational induction of endonuclease inhibition by cationic triplatin complexes. *Nucleic Acids Res* 2014;**42**:13474–87. https://doi.org/10.1093/nar/gku1157
13. Qu Y, Kipping RG, Farrell NP. Solution studies on DNA interactions of substitution-inert platinum complexes mediated via the phosphate clamp. *Dalton Trans* 2015;**44**:3563–72. https://doi.org/10.1039/C4DT03237C
14. Wedlock LE, Kilburn MR, Liu R *et al.* NanoSIMS multi-element imaging reveals internalisation and nucleolar targeting for a highly-charged polynuclear platinum compound. *Chem Commun* 2013;**49**:6944–6. https://doi.org/10.1039/c3cc42098a
15. Peterson EJ, Menon VR, Gatti L *et al.* Nucleolar targeting by platinum: p53-independent apoptosis follows rRNA inhibition, cell-cycle arrest, and DNA compaction. *Mol Pharmaceutics* 2015;**12**:287–97. https://doi.org/10.1021/mp5006867
16. Benedetti BT, Peterson EJ, Kabolizadeh P *et al.* Effects of noncovalent platinum drug-protein interactions on drug efficacy: use of fluorescent conjugates as probes for drug metabolism. *Mol Pharmaceutics* 2011;**8**:940–8. https://doi.org/10.1021/mp2000583
17. Wirth R, White JD, Moghaddam AD *et al.* Azide vs alkyne functionalization in Pt(II) complexes for post-treatment click modification: solid-state structure, fluorescent labeling, and cellular fate. *J Am Chem Soc* 2015;**137**:15169–75. https://doi.org/10.1021/jacs.5b09108
18. White JD, Guzman LE, Zakharov LN *et al.* An alkyne-appended, click-ready PtII complex with an unusual arrangement in the solid State. *Angew Chem Int Ed* 2015;**54**:1032–35. https://doi.org/10.1002/anie.201409853
19. White JD, Osborn MF, Moghaddam AD *et al.* Picazoplatin, an azide-containing platinum(II) derivative for target analysis by click chemistry. *J Am Chem Soc* 2013;**135**:11680–3. https://doi.org/10.1021/ja402453k
20. Jiang K, Humbert N, Kk S *et al.* Annealing of ssDNA and compaction of dsDNA by the HIV-1 nucleocapsid and gag proteins visualized using nanofluidic channels. *Quart Rev Biophys* 2019;**52**:e2. https://doi.org/10.1017/S0033583518000124
21. KK S, Ekedahl E, Hoang NTB *et al.* High diversity of blaNDM-1-encoding plasmids in *Klebsiella pneumoniae* isolated from neonates in a Vietnamese hospital. *Int J Antimicrob Agents* 2022;**59**:106496. https://doi.org/10.1016/j.ijantimicag.2021.106496
22. KK S, Sewunet T, Wangchinda W *et al.* Optical DNA mapping of plasmids reveals clonal spread of carbapenem-resistant *Klebsiella pneumoniae* in a large Thai hospital. *Antibiotics* 2021;**10**:1029. https://doi.org/10.3390/antibiotics10091029
23. Frykholm K, Müller V, Kk S *et al.* DNA in nanochannels: theory and applications. *Quart Rev Biophys* 2022;**55**:e12. https://doi.org/10.1017/S0033583522000117
24. Öz R, Kk S, Westerlund F. A nanofluidic device for real-time visualization of DNA–protein interactions on the single DNA molecule level. *Nanoscale* 2019;**11**:2071–8.https://doi.org/10.1039/C8NR09023H
25. Dvirnas A, Pichler C, Stewart CL *et al.* Facilitated sequence assembly using densely labeled optical DNA barcodes: a combinatorial auction approach. *PLoS One* 2018;**13**:e0193900. https://doi.org/10.1371/journal.pone.0193900
26. Haynes PJ, Main KHS, Akpinar B *et al.* Atomic force microscopy of DNA and DNA–protein interactions. In: Leake MC (ed.), *Chromosome Architecture: Methods and Protocols*. New York, NY: Humana, 2022, 43–62. https://doi.org/10.1007/978-1-0716-2221-6_5
27. Beton JG, Moorehead R, Helfmann L *et al.* TopoStats – A program for automated tracing of biomolecules from AFM images. *Methods* 2021;**193**:68–79. https://doi.org/10.1016/j.ymeth.2021.01.008
28. Hampton JD, Peterson EJ, Katner SJ *et al.* Exploitation of sulfated glycosaminoglycan status for precision medicine of triplatin in triple-negative breast cancer. *Mol Cancer Ther* 2022;**21**:271–81. https://doi.org/10.1158/1535-7163.MCT-20-0969
29. Kauffman GB. Il'ya Il'ich Chernyaev (1893-1966) and the trans effect. *J Chem Educ* 1977;**54**:86. https://doi.org/10.1021/ed054p86
30. Nyberg LK, Persson F, Berg J *et al.* A single-step competitive binding assay for mapping of single DNA molecules. *Biochem Biophys Res Commun* 2012;**417**:404–8. https://doi.org/10.1016/j.bbrc.2011.11.128
31. KK S, Wranne MS, Sewunet T *et al.* Identification and characterization of plasmids carrying the mobile colistin resistance gene mcr-1 using optical DNA mapping. *JAC Antimicrob Resist* 2023;**5**:dlad004. https://doi.org/10.1093/jacamr/dlad004
32. Seidel SAI, Dijkman PM, Lea WA *et al.* Microscale thermophoresis quantifies biomolecular interactions under previously challenging conditions. *Methods* 2013;**59**:301–15. https://doi.org/10.1016/j.ymeth.2012.12.005

33. McGorman B, Poole S, López MV *et al.* Analysis of non-canonical three- and four-way DNA junctions. *Methods* 2023;**219**:30–8. https://doi.org/10.1016/j.ymeth.2023.09.002
34. Malina J, Farrell NP, Brabec V. Substitution-inert trinuclear platinum complexes efficiently condense/aggregate nucleic acids and inhibit enzymatic activity. *Angew Chem Int Ed* 2014;**53**:12812–6. https://doi.org/10.1002/anie.201408012
35. Hou XM, Zhang XH, Wei KJ *et al.* Cisplatin induces loop structures and condensation of single DNA molecules. *Nucleic Acids Res* 2009;**37**:1400–10. https://doi.org/10.1093/nar/gkn933
36. Burgess DJ, Doles J, Zender L *et al.* Topoisomerase levels determine chemotherapy response *in vitro* and *in vivo*. *Proc Natl Acad Sci USA* 2008;**105**:9053–8. https://doi.org/10.1073/pnas.0803513105
37. Peixoto P, Bailly C, David-Cordonnier M-H. Topoisomerase I-mediated DNA relaxation as a tool to study intercalation of small molecules into supercoiled DNA. In: Fox KR (ed.), *Drug–DNA Interaction Protocols*. New York, NY: Humana, 2010, 235–56.
38. Predarska I, Saoud M, Morgan I *et al.* Cisplatin-cyclooxygenase inhibitor conjugates, free and immobilised in mesoporous silica SBA-15, prove highly potent against triple-negative MDA-MB-468 breast cancer cell line. *Dalton Trans* 2022;**51**:857–69. https://doi.org/10.1039/D1DT03265H
39. Bianchini G, De Angelis C, Licata L *et al.* Treatment landscape of triple-negative breast cancer–expanded options, evolving needs. *Nat Rev Clin Oncol* 2022;**19**:91–113. https://doi.org/10.1038/s41571-021-00565-2
40. Dutta S, Rivetti C, Gassman NR *et al.* Analysis of single, cisplatin-induced DNA bends by atomic force microscopy and simulations. *J Molecular Recognition* 2018;**31**:e2731. https://doi.org/10.1002/jmr.2731
41. Li L, Liu R, Xu F *et al.* Study on the interactions between anti-cancer drug oxaliplatin and DNA by atomic force microscopy. *Micron* 2015;**76**:46–51. https://doi.org/10.1016/j.micron.2015.05.002

Received: October 15, 2024. **Revised:** June 11, 2025. **Editorial Decision:** June 11, 2025. **Accepted:** June 23, 2025